ARKIV FÖR FYSIK Band 14 nr 16

Communicated 4 June 1958 by H. ALFVÉN and N. HERLOFSON

The optics of cosmic ray telescopes[1]

By ERNST-ÅKE BRUNBERG

With 42 figures in the text

Contents

Abstract 196
Introduction 196
Presentation of the problem and definition of cosmic ray image 197
1. *Geomagnetic deflection of primary cosmic ray particles* 198
1.1. Discussion of the primary particle flow 198
1.2. The element in phase space representing a telescope 199
1.3. The transformation of solid angle and surface of a telescope 202
1.4. The properties of a telescope of finite dimensions 203
1.4.1. The general case 203
1.4.2. The narrow angle telescope 205
1.4.3. The ionization chamber 205
1.4.4. The three dimensional polar diagram of a telescope on the sphere of asymptotic directions 206
1.4.5. A few examples of calculating polar diagrams when the atmospheric influence is neglected 206
2. *The influence of the atmosphere* 210
2.1. The spread in the atmosphere 211
2.1.1. The rate of inelastic nucleon-nucleon collisions in the atmosphere 211
2.1.2. The intensity and energy distributions of π-mesons produced in nucleon-nucleon collisions 218
2.1.3. Different processes influencing the intensity and energy distributions of mesons 220
2.1.3.1. The $\pi \rightarrow \mu$ decay 220
2.1.3.2. The decay and absorption of μ-mesons 222
2.1.3.3. Scattering of μ-mesons 225
2.1.3.4. Magnetic deflection of the μ-mesons in the atmosphere . . . 227
2.2. The polar diagram of telescopes of finite dimensions when the geomagnetic influence on the primary particles is neglected 235
2.3. The zenith angle dependence of the radiation at sea level. 240
3. *The complete polar diagram of a cosmic ray telescope* 241
3.1. The image of a source element obtained by using the polar diagram . . 244
4. *The resolving power of cosmic ray telescopes* 244
APPENDIX
AI. Calculation of the effective measuring surface of cylindrical telescopes 248

(¹) A preliminary report on this work was given by the author at the "IUPAP. Cosmic Ray Conference" at Varenna in June 1957.

AII. The total production rate of secondaries in the atmosphere 249
AIII. Intensity and energy distributions of π-mesons produced in nucleon-nucleon collisions 250
AIV. The counting rate of cylindrical telescopes assuming a $\cos^2 \beta$ distribution of the intensity 252
AV. Magnetic deflection of secondary cosmic ray particles in the atmosphere. By BJÖRN BONNEVIER 255

ACKNOWLEDGEMENTS 261

REFERENCES 261

ABSTRACT

The directional properties of cosmic ray telescopes are analyzed with regard to both geomagnetic deflection of the primary particles and to the spread in the atmosphere of the secondaries.

The concepts "image of a cosmic ray source" and "polar diagram of a telescope outside the earth's magnetic field" are introduced. Image of a cosmic ray source is defined as the intensity variation recorded by a telescope during one day. The polar diagram represents the sensitivity of a telescope for different angular positions of a cosmic ray source element on the celestial sphere.

A few examples of calculating polar diagrams are given. The resolving power of cosmic ray telescopes is discussed.

INTRODUCTION

The purpose of measuring the extra-terrestrial intensity variation of the cosmic radiation is to find the positions of cosmic ray sources in space as well as to study the influence of cosmical electric and magnetic fields on the particles and thus explore the electromagnetic state within the planetary system. All this can be looked upon as the problem of finding the shape and strength of a cosmic ray source located far away from the earth.

The measurements are usually carried out with Geiger-Müller tube telescopes, ionization chambers and neutron recording instruments. Telescopes measure radiation coming from directions within a rather narrow cone and have a higher resolving power than ionisation chambers and neutron recording instruments, which in principle are omnidirectional. Owing to atmospheric absorption, however, particles arriving in the zenith direction contribute more to the counting rate than particles from other directions, a fact which gives the omnidirectional instruments properties similar to those of broad angle telescopes pointing in the zenith direction.

If observations are carried out using only one telescope with a well defined measuring direction the information derived when the earth rotates is limited to a narrow annular region centred around the earth's axis. In order to get more information about the cosmic ray intensity distribution in space we must use several telescopes at different latitudes with each telescope scanning a certain region around the earth's axis. This can also be achieved with telescopes pointing in different zenith- and azimuth directions at the same place on the earth. The most suitable locations and directions of measurement depend on the deflection of the primary cosmic ray particles in the geomagnetic field.

Presentation of the problem and definition of cosmic ray image

In general the cosmic ray source viewed from the earth extends over a certain region of the celestial sphere and the particle intensity varies over this region. Suppose that the angular extension of the source and the distribution of the particle intensity on the celestial sphere as well as the differential momentum spectrum of the particles are given.

We want to know the intensity variation recorded by a cosmic ray telescope at a given place on the earth pointing in a given direction when the earth rotates and the telescope thus scans a certain region of the source as in fig. 1.

The intensity variation recorded by the telescope during one day is called *the image of the cosmic ray source* in the following. When the cosmic ray source is fixed on the celestial sphere the image is the variation recorded during a *sideral* day. If, on the other hand, the cosmic ray source is related to phenomena within the solar system and gives an intensity variation with solar time the image is the variation recorded during a *solar* day. In the latter case the source moves on the celestial sphere. The aim of the present paper is to show how the image is influenced by the geomagnetic deflection of the primary particles and by the different processes

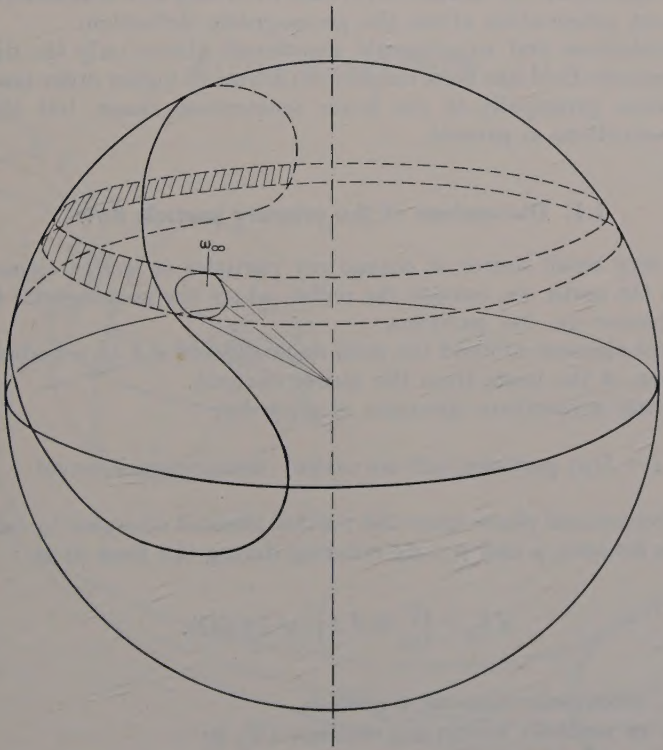

Fig. 1. The extension of a cosmic ray source on the celestial sphere is the region enclosed by the curve on the left of the figure. The particle intensity along the dashed strip of the source is recorded by the telescope when the earth rotates. ω_∞ is the measuring solid angle of the telescope outside the earth's magnetic field.

occurring in the atmosphere. The optics of cosmic ray telescopes thus includes a study of these two main parts as well as the influence of the geometrical dimensions of the telescope itself.

In order to find the image of a cosmic ray source we start by finding the image of a source element subtending an infinitely small solid angle. Using the results of this study it is then possible to deduce the image of any extended cosmic ray source.

The problem is divided into two main parts: a study of the deflection of the primary particles in the geomagnetic field and the influence of the atmosphere upon the particle flow. Variations in atmospheric conditions which introduce variations in cosmic ray intensity are, however, not considered in this paper.

1. GEOMAGNETIC DEFLECTION OF PRIMARY COSMIC RAY PARTICLES

Our knowledge in this field is extensive (although not yet sufficient) thanks to the mathematical calculations by Störmer [1], Lemaître and Vallarta [2], Firror [3], Jory [4], Lüst, Schlüter and Katterbach [5], Lüst [6] and many others [cf. 7, 8]. Scale model experiments by Malmfors [9] and Brunberg and Dattner [10] have also given important information about the geomagnetic deflection.

In the calculations and experiments mentioned above, only the dipole term of the earth's magnetic field has been considered. Terms of higher order may necessitate small corrections, principally in the lower momentum range, but little is known about these corrections at present.

1.1. Discussions of the primary particle flow

Consider a very small source of cosmic ray particles (a source element) situated far away from the earth, i.e. outside the region where the geomagnetic field has any deflecting influence on the particles.

Let the source element subtend the solid angle $d\Omega$ and dA be a surface element in the cross-section of the beam from the source element.

The differential momentum spectrum is given by:

$$I = I(p) \text{ particles/cm}^2\cdot\text{sec}\cdot\text{sterad}\cdot\text{momentum interval.}$$

In the six-dimensional phase space the volume element occupied by beam particles with momenta between p and $p + dp$ entering during the time dt is:

$$d V_p = \left(\frac{p}{m}\, dt\, dA\right) (p^2\, dp\, d\Omega). \tag{1}$$

m denotes the relativistic mass of a particle.

The number of particles within the element $d V_p$ is:

$$dN = I(p)\, dp\, dA\, d\Omega\, dt. \tag{2}$$

Consequently the density of particles in phase space is:

$$D = \frac{dN}{dV_p} = \frac{I(p)\,dp}{p^3}\,m. \tag{3}$$

Liouville's theorem of statistical mechanics shows that the density of particles within the element dV_p is constant when the element moves about in phase space. This has been pointed out by Lemaître and Vallarta [11] and further treated by Swann [12]. Thus particles originating from a surface element dA of the primary beam form a tube of flow in phase space with a particle density given by eq. 3. Compare also Jánossy [13, p. 266].

As dA and $d\Omega$ are infinitely small the tube of flow is infinitely thin. The flow pattern is governed by the geomagnetic deflection.

1.2. The element in phase space representing a telescope

We consider a telescope on the earth with infinitely small solid angle $d\omega$ around $\mathbf{p}_T$ and surface da perpendicular to $\mathbf{p}_T$, where the vector $\mathbf{p}_T$ represents the measuring direction of the telescope, see fig. 2.

The six-dimensional element dV_T in phase space contains the number of particles with momenta between p_T and $p_T + dp_T$ which are recorded by the telescope during the time dt. In the following dV_T is called the telescope element in phase space and is given by:

$$dV_T = \frac{p_T}{m}\,dt\,da\,p_T^2\,dp_T\,d\omega. \tag{4}$$

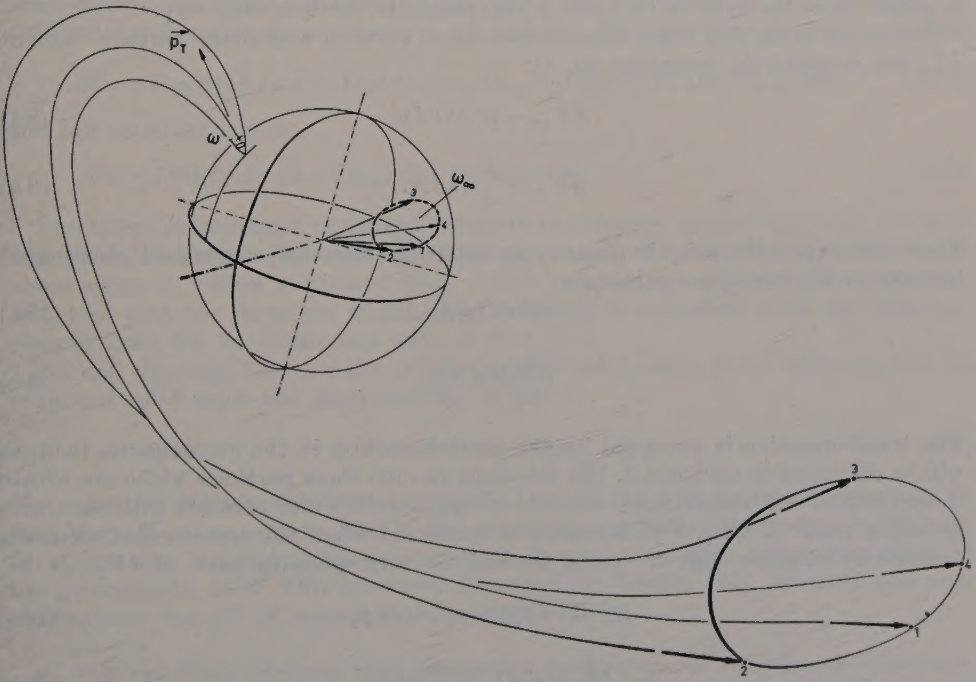

Fig. 2. The projection of the solid angle ω of a telescope located on the earth. The direction of the axis of the telescope is defined by $\mathbf{p}_T$. The projection is carried out by means of particle orbits in the geomagnetic field and the projected solid angle ω_∞ is visualized on the sphere.

The position of $d\,V_T$ in phase space changes with the direction of $\mathbf{p}_T$ and is consequently dependent both on time (as the earth rotates) and the measuring zenith and aximuth directions of the telescope. When the telescope element is completely inside the particle flow in phase space, as regards both its momentum and three dimensional space parts, the number of particles within the element is:

$$dn = D\,d\,V_T, \tag{5}$$

where D is given by eq. 3.

As the particle energy is constant in the magnetic field we have $p = p_T$. From this and equations (3), (4) and (5) the number of particles recorded by the telescope per unit time is:

$$d^3\nu = dn/dt = I(p)\,dp\,da\,d\omega \quad \text{particles/sec.}^{(1)} \tag{6}$$

From eq. 6 we conclude that a telescope measures the same intensity in the geomagnetic field as another telescope would measure outside the geomagnetic field, provided that the particle flow covers the surfaces and solid angles of the telescopes and that the product of the solid angle and surface of the two telescopes are equal. This means that:

$$da\,d\omega = da_\infty\,d\omega_\infty, \tag{7}$$

where da_∞ and $d\omega_\infty$ are the surface and solid angle respectively of a telescope outside the geomagnetic field.

The condition that the telescope element $d\,V_T$ must lie completely inside the flow in phase space for eq. 6 to be valid is interpreted in the following way:

The momentum and three-dimensional space parts of a primary particle element $d\,V_p$ are respectively (compare eq. 1):

$$d\,V_{pm} = p^2\,d\Omega\,dp, \tag{8a}$$

$$d\,V_{ps} = \frac{p}{m}\,dt\,dA. \tag{8b}$$

The motion up to the point in phase space where the telescope element $d\,V_T$ is situated transforms the two space parts into:

$$(p^2\,d\Omega\,dp)_T, \tag{9a}$$

$$\left(\frac{p}{m}\,dt\,dA\right)_T. \tag{9b}$$

The transformation is governed by the particle motion in the geomagnetic field, as will be discussed in section 1.3. The telescope records those particles which are within those parts of the transformed elements of equations 9 which coincide with the corresponding parts of $d\,V_T$. Full intensity is measured when the transformed elements completely coincide with or extend beyond the corresponding parts of $d\,V_T$:

$$(p^2\,d\Omega\,dp)_T \geqslant {p_T}^2\,d\omega\,dp_T, \tag{10a}$$

$$\left(\frac{p}{m}\,dt\,dA\right)_T \geqslant \frac{p_T}{m}\,dt\,da, \tag{10b}$$

---

(1) The number 3 denotes the order of the differential.

or as $p_T = p$:
$$d\Omega_T \geqslant d\omega, \tag{11a}$$
$$dA_T \geqslant da. \tag{11b}$$

The condition of coincidence naturally requires:

1) That the whole range of directions of particle motion at the telescope completely covers or extends beyond the solid angle of the telescope.
2) That the transformed surface element of the cross-section of the beam completely covers or extends beyond the surface of the telescope.

As will be shown later it is more convenient from the practical point of view to go the other way and transform the telescope element from the earth to infinity. A discussion similar to the one above then gives instead of equations 11a and 11b:

$$d\Omega \geqslant d\omega_\infty, \tag{12a}$$
$$dA \geqslant da_\infty. \tag{12b}$$

The condition of coincidence is then that the whole range of directions of particle motion in the primary beam completely covers or extends beyond the transformed solid angle $d\omega_\infty$. Eq. 12b is always fulfilled as the cross-section of the primary beam was assumed to be very large.

We thus summarize that a telescope with infinitely small solid angle and surface records full particles intensity from the momentum interval dp in a beam of large cross-section subtending the solid angle $d\Omega$ when the condition of coincidence is fulfilled together with the equations 7, 12a and 12b. The counting rate is derived from:

$$d^3\nu = I(p)\,dp\,da\,d\omega = I(p)\,dp\,da_\infty d\omega_\infty = I(p)\,dp\,da\,(d\omega/d\omega_\infty)\,d\omega_\infty, \tag{13a}$$

and full counting rate is:

$$d^3\nu = I(p)\,dp\,da\,(d\omega/d\omega_\infty)\,d\Omega \text{ particles/sec.} \tag{13b}$$

The telescope measures either full intensity or nothing, when considering particles in a given momentum interval. Full intensity means that the telescope element in phase space is within a tube of flow, which happens when the direction of $d\omega_\infty$ coincides with the direction of $d\Omega$. Zero intensity is measured when the telescope element does not lie within any tube of flow.

We call the ratio between the infinitely small solid angle of the telescope and its projected solid angle the magnification M:

$$M = d\omega/d\omega_\infty. \tag{14}$$

For infinitely high momenta it is evident that $M = 1$ but for lower momenta we may have $M > 1$ as well as $M < 1$. For certain momenta and geomagnetic latitudes M approaches infinitely high values which is connected with a focusing effect in the geomagnetic field. This has been discussed by Åström [14]. At momenta near geomagnetic cut-off M approaches zero.(1)

---

(1) This was clearly observed when determining the geomagnetic deflection experimentally, Brunberg and Dattner [10]. The luminous spot on the fluorescent screen, which for high momenta was approximately 2 cm², increased enormously near the cut-off momenta. The surface of the spot could be used for an accurate determination of M.

We have, from equations 12b, 13a and 14:

$$dA = da\,(d\omega/d\omega_\infty) = da\,M, \tag{15}$$

i.e. the surface element dA which completely coincides with da_∞ depends on M and, consequently, so does the counting rate when the primary beam subtends an infinitely small solid angle but has infinite extension.(¹)

In the case when particles are moving isotropically in space around the earth, a telescope always measures the same intensity because the particle flow covers the projected surface and solid angle of a telescope for any allowed transformation through the geomagnetic field. This was first pointed out by Lemaître and Vallarta [11].

1.3. The transformation of solid angle and surface of a telescope

The transformations or projections are carried out along the particle orbits in the geomagnetic field. The direction of orbits far away from the earth are called asymptotic directions. They are represented by vectors emanating from the centre of a globe and the direction of a vector is defined by the geographic latitude and longitude angles Φ and Ψ. The longitude angle is reckoned east from the meridian plane through the point where the particle orbit hits the earth. On the globe surface the end points of the vectors give the asymptotic directions for different particle momenta, and measuring directions on the earth. End points corresponding to different particle momenta but to the same measuring direction are joined, giving a curve on the globe. The curves for different measuring directions are used to find the projected solid angle of a given telescope as described by Brunberg [15].

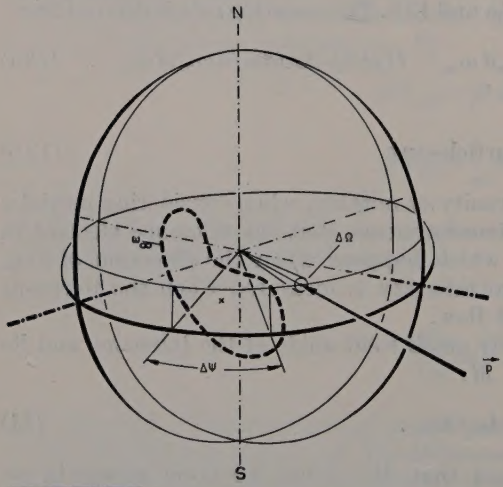

Fig. 3. The sphere of asymptotic directions. p denotes the angular position of the source, from which particles of momentum p arrive, within the small solid angle $\Delta\Omega$. The area on the sphere enclosed by the dashed line represents the projected solid angle ω_∞ of a telescope on the earth.

(¹) This is in accordance with the general optical law of Helmholtz which, applied to particle motion in electric and magnetic fields, states that:

$$v_0^2 \cos\vartheta_0\, dF_0\, d\Omega_0 = v_1^2 \cos\vartheta_1\, dF_1\, d\Omega_1,$$

where v = the particle velocity, dF = a surface element of the particle beam, $d\Omega$ = the solid angle subtended by the beam, and ϑ = the angle between the normal of the surface, dF, and the direction of the beam. Subscripts refer to different positions along the beam (see Glaser (1951), *Grundlagen der Elektronenoptik*, p. 623).

In our case we have $v_0 = v$ and $\cos\vartheta = 1$. Consequently:

$$dF_1/dF_0 = d\Omega_0/d\Omega_1 = M.$$

Fig. 2 shows the projection of a finite solid angle of a telescope for a given particle momentum. In the following such a globe will be referred to as a sphere of asymptotic directions. The coincidence of the primary particle flow and the projected finite solid angle of a telescope is easily visualized on the sphere, as shown in fig. 3, and is further treated in section 1.4.

1.4. The properties of a telescope of finite dimensions

In the preceding sections the recording properties of a telescope with infinitely small solid angle and surface have been discussed. Consider now a cylindrical telescope bounded by two circular surfaces, *a*, separated by a distance, *d*, as in fig. 4.

1.4.1. *The general case*

The counting rate of the telescope is (from eq. 6):

$$d\nu = I(p)\,dp \int_a \int_\omega da\, d\omega. \tag{16}$$

Eq. 16 means an integration in phase space over all telescope elements $d V_T$ which are completely within the particle flow and thus contribute to the counting rate. Let us first consider the integration over the solid angle in eq. 16 and find the intensity recorded by a surface element da and the whole solid angle ω_0 of the telescope belonging to da.

Using equations 13a and 14 we have the following expression for the number of particles recorded by a surface element da of the given telescope:

$$d^2\nu = I(p)\,dp\,da \int_{(\omega_0)_\infty} \cos u\, M\, d\omega_\infty, \tag{17}$$

where $(\omega_0)_\infty$ is the projection of the solid angle ω_0 on the sphere of asymptotic directions. (da cos u) is the projected area of da on a plane perpendicular to the direction

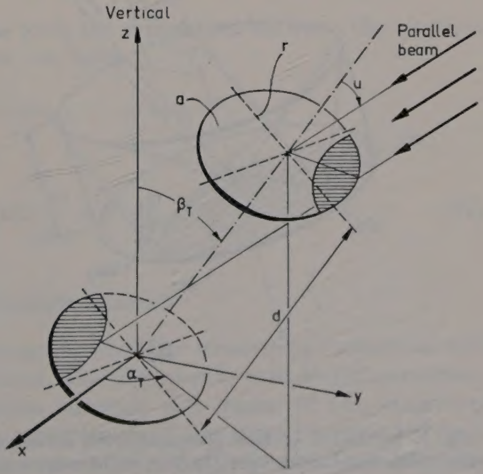

Fig. 4. A cylindrical telescope bounded by two circular surfaces separated by a distance *d*. The shaded area is the recording part of the surface for particles arriving at an angle *u* to the axis of the telescope.

of particles arriving at the telescope. Contributious to the integral come only from the part of the solid angle which contains sources; consequently:

$$\int_{(\omega_0)_\infty} \cos u\, M\, d\omega_\infty = \int_\varepsilon \cos u\, M\, d\Omega,$$

where ε is the extension of the source within $(\omega_0)_\infty$. Thus the integration over the solid angle of the telescope is replaced by an integration over the solid angle part of the source which is within the projected solid angle of the telescope on the sphere of asymptotic directions. The counting rate due to a source element $d\Omega$ within the projected solid angle is:

$$d^3\nu = I(p)\,dp\,da \cos u\, M\, d\Omega. \tag{18a}$$

As we shall discuss the counting rate of a telescope due to a source subtending a small solid angle we introduce in the following, for the sake of simplicity, a source element subtending the small but finite solid angle $\Delta\Omega$. As M and u are assumed to be constant over the source, integration of eq. 18a gives:

$$d^2\nu = I(p)\,dp\,da \cos u\, M\, \Delta\Omega. \tag{18b}$$

Fig. 5*a* shows the situation. Three surface elements in a telescope are drawn as an example with their corresponding solid angles ω_1, ω_2 and ω_3. The corresponding solid angles on the sphere of asymptotic directions are shown in fig. 5*b*. The dashed curve is the limit of projected solid angles belonging to surface elements on the fringe of the lower telescope surface. The *total* solid angle of the telescope is defined by the apex angle $2\,u_{\max}$ with $u_{\max} = \text{arc tg}(2r/d)$ and equals $2\pi(1-\cos u_{\max})$, see fig. 4. The position of $\Delta\Omega$ on the sphere indicates the angular position of the source element and determines the angles of incidence at the telescope. u is the angle between

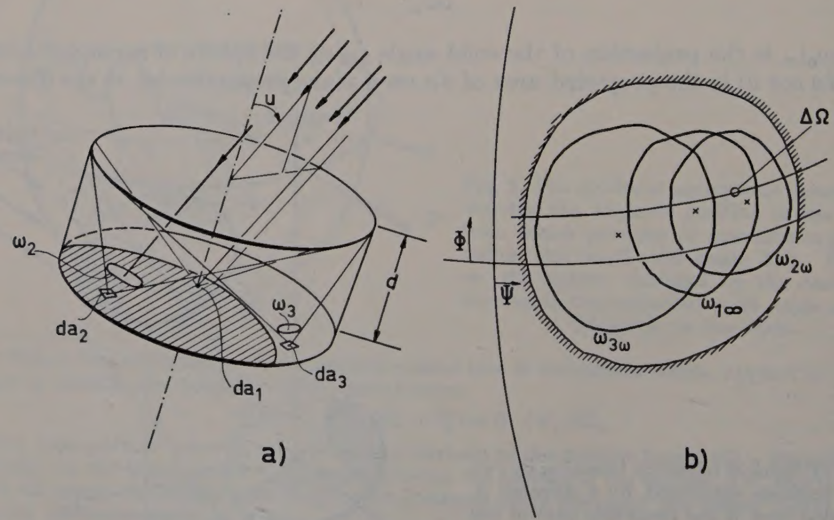

Fig. 5. (*a*) Three surface elements with corresponding solid angles are chosen as an example in the cylindrical telescope. (*b*) The solid angles projected on the sphere of asymptotic directions.

the central telescope direction and the direction of arriving particles. According to equation 18b the surface elements da_1 and da_2 contribute to the counting rate by:

$$d^2\nu_1 = I(p)\,dp\,da_1 \cos u\, M\,\Delta\Omega, \tag{19a}$$

$$d^2\nu_2 = I(p)\,dp\,da_2 \cos u\, M\,\Delta\Omega, \tag{19b}$$

whereas there is no contribution from da_3.

The surface integral yields:

$$d\nu = I(p)\,dp\,a \cos u\, G(u)\, M\,\Delta\Omega. \tag{20}$$

$G(u)$ is a function determined by the geometry of the telescope and takes into account the fact that only a part of the surface records particles arriving from the direction defined by the angle u. This part is shaded in fig. $5a$ where the surface element da_3 is outside the recording region. As mentioned above, u is a function of the positional angles Φ and Ψ of the source element on the sphere of asymptotic directions. The function $\cos u\, G(u)$ is calculated in appendix I for cylindrical telescopes of different apertures. As the magnification M depends on the orbits in the magnetic field it is a function both of the particle momentum and the angular position of the source element.

The sphere of asymptotic directions is used when calculating the counting rate of a telescope when the earth rotates relative to the source element. The total solid angle of the telescope is projected on the sphere using particle orbits corresponding to the momentum p as in fig. 3. The direction to the source element is given by the vector $\mathbf{p}$ and the source subtends the solid angle $\Delta\Omega$. When the earth rotates $\Delta\Omega$ moves along a parallel circle on the sphere. In the angular interval $\Delta\Psi$ the counting rate of the telescope is determined by eq. 20. In this way it is possible to calculate the counting rate due to different parts of the source spectrum for any angular position (Φ,Ψ) of the source element. The total counting rate of the telescope is obtained by adding the contributions from all parts of the spectrum.

1.4.2. *The narrow angle telescope*

For small values of ω, i.e. for telescopes with the separation between the surfaces large compared to the radius of a surface, we have:

$$\cos u \approx 1, \qquad M \approx \omega/\omega_\infty, \qquad \omega \approx a/d^2.$$

The counting rate is from eq. 20:

$$d\nu \approx I(p)\,dp\,\Delta\Omega\,\frac{\omega}{\omega_\infty}\,a\,G(u). \tag{21}$$

1.4.3. *The ionization chamber*

In a spherical ionization chamber the magnitude of the measuring surface as well as the solid angle is the same in all directions. The chamber is said to be omnidirectional. The measuring surface (cross-section through the centre of the chamber) perpendicular to the direction of arriving particles shall of course be regarded as a fictious one as the particles ionize along their whole path within the chamber. Particles passing through the centre of the surface consequently contribute more to the recorded intensity than other particles. But this variation of sensitivity over a cross-section of the chamber does not complicate the calculations as it is the same in all measuring directions. The counting rate according to eq. 20 with $G(u) = 1$ is:

$$d\nu = I(p)\,dp\,\Delta\Omega\,M\,a_e, \tag{22}$$

where a_e is the effective measuring surface of the chamber.

When calculating the counting rate of the chamber, its solid angle, 2π (only the upper half sphere) is projected on the sphere of asymptotic directions. As long as the angular position of the source element is within the projected solid angle the counting rate is given by eq. 22.

1.4.4. *The three-dimensional polar diagram of a telescope on the sphere of asymptotic directions*

The counting rate of a telescope is calculated according to section 1.4.1 for different angular positions of the source element represented by the solid angle $\Delta\Omega$ on the sphere of asymptotic directions and assuming a certain momentum spectrum. Each position of the element gives a certain counting rate in the telescope for a given momentum interval—the sensitivity of the telescope varies with the position of $\Delta\Omega$. At every position of $\Delta\Omega$ we mark out a distance in the radial direction proportional to the counting rate of the telescope with $\Delta\Omega$ in this position. This gives a curved surface above the globe surface, the height of which varies continuously over the globe. This "mountain" is the three-dimensional polar diagram of the telescope in the given momentum interval. The total three-dimensional polar diagram is suitably found by dividing the whole spectrum into a number of finite momentum intervals Δp and calculating the curved surface given by each interval. The geomagnetic deflection of particles within an interval is then represented by the mean value of p in that interval. Superposition of the contributions from the whole spectrum constitutes the total three-dimensional polar diagram of the telescope on the sphere of asymptotic directions.

In the following, a section along a parallel circle of the curved surface will be used. This represents the counting rate of the telescope as a function of Ψ, i.e. the longitudinal position of the source reckoned to the east from the meridian plane through the place of observation on the earth. This section is important in the following discussions and is referred to as the polar diagram of the telescope along the parallel circle in question.

1.4.5. *A few examples of calculating polar diagrams when the atmospheric influence is neglected*

We shall now discuss the calculation of polar diagrams of an ionization chamber and of cylindrical telescopes with different apertures but with the same surfaces. The telescopes point in the zenith direction and their geometrical configuration is shown in fig. 4 where now $\beta_T = 0$.

The angular position of the source is along a parallel circle on the geographic latitude Φ and the beam from the source subtends the small solid angle $\Delta\Omega$. The source spectrum used is the same as that of the isotropic background which seems

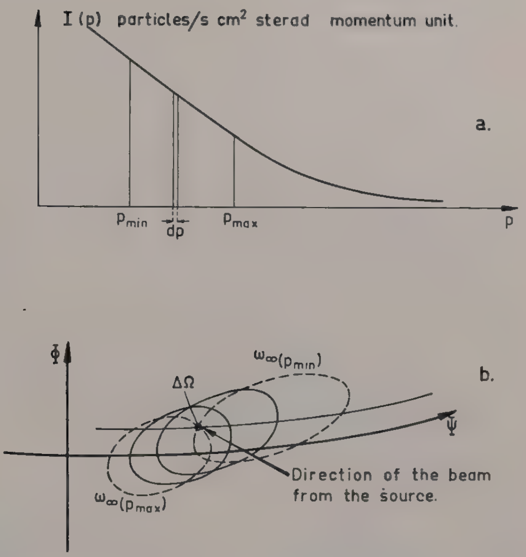
I (p) particles/s cm² sterad momentum unit.
a.
p_min
dp
p_max
p
Φ
ω∞(p_min)
ΔΩ
b.
Ψ
Direction of the beam from the source.
ω∞(p_max)

Fig. 6. (*a*) The primary differential momentum spectrum schematically drawn. (*b*) The positions of the projected solid angle for different primary momenta.

reasonable in this first approach. The differential spectrum adopted is proportional to p^{-2}, cf. [46].

The total solid angle of the telescope which corresponds to the apex angle $2\,u_{\max}$ is projected on the sphere of asymptotic directions. This is done for different momenta, each of them representing a certain momentum interval dp. The projected total solid angle on the sphere contains all possible directions of incidence at the telescope for momenta between p and $p+dp$. When the angular position of the source element is within the projected solid angle the counting rate due particles in the momentum interval dp is given by eq. 20.

For a certain angular position of the source element the total counting rate is:

$$\nu = a\,\Delta\Omega \int_{p_{\min}}^{p_{\max}} M \cos u\, G(u)\, I(p)\, dp. \tag{23}$$

$p_{\min}$ and $p_{\max}$ are the minimum and maximum momenta for which the corresponding projected solid angles contain the source element on the sphere of asymptotic directions. This is shown schematically in fig. 6. The counting rate is computed for a number of source positions along the parallel circle $\Phi = \text{const.}$ and the counting rate thus obtained as a function of the longitudinal angle Ψ is the polar diagram of the telescope along this parallel circle.

In the following the spectrum has been divided into a number of finite intervals Δp with each interval centred at a momentum p_i. The number of particles within that interval, $I(p_i)\,\Delta p$, are taken as having the same deflection represented by the momentum p_i and their asymptotic directions are within the corresponding solid angle on the sphere of asymptotic directions, fig. 7*a* and *b*.

For each position of $\Delta\Omega$ on the sphere the counting rate due to particles in the momentum interval between p_i and $(p_i + \Delta p)$ is:

$$\Delta\nu_i = a\,\Delta\Omega\, I(p_i)\,\Delta p\, M_i \cos u_i\, G(u_i). \tag{24}$$

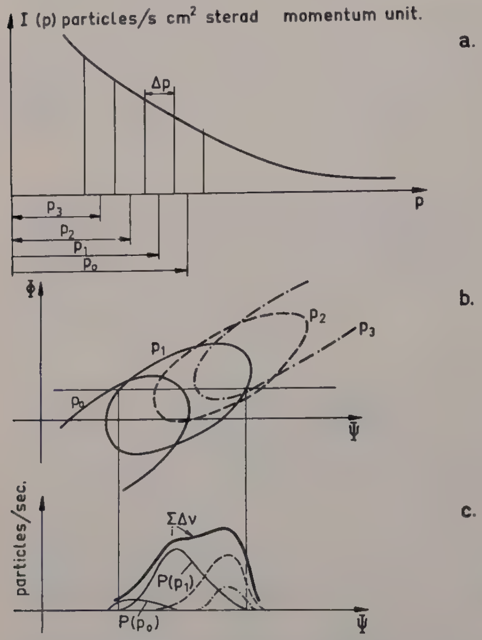

Fig. 7. The principle of calculating a pola-diagram along a parallel circle. (*a*) The primary differential momentum spectrum. (*b*) The projected solid angle for different momenta. (*c*) The polar diagram along a parallel circle.

The magnification M and the angle of incidence (α,β) at the telescope are found from the sphere. As regards the angles, only the zenith angle β matters in this exampel because the central direction of the telescope points in the zenith direction, from which it follows that $u=\beta$. The counting rate is thus written:

$$\Delta\nu_i = a\,\Delta\Omega\, I(p_i)\,\Delta p\, \mathrm{M}_i \cos\beta_i\, G(\beta_i). \tag{25}$$

$\cos\beta\, G(\beta)$ has been calculated in appendix I.

The counting rate of an ionization chamber is (compare eq. 22):

$$\Delta\nu_i = a_e\,\Delta\Omega\, I(p_i)\,\Delta p\, M_i. \tag{26}$$

The counting rate is computed in this way for a number of angular positions Ψ of the source within the total solid angle and plotted as a function of Ψ, see fig. 7*b*, *c*. The polar diagram thus obtained (for instance $P(p_1)$ in fig. 7*c*) is approximately that corresponding to particles in the momentum interval between $(p_1 - \frac{1}{2}\Delta p)$ and $(p_1 + \frac{1}{2}\Delta p)$.

The approximation is naturally better the smaller Δp, but as the accuracy of the projected solid angles amounts to 4°–5° in position, sometimes more, this puts a lower limit to Δp. The limit value could, however, be increased still more as, in reality, the measured counting rate is the averge taken over a considerable time, usually two hours, which corresponds to a change of 30° in the position of $\Delta\Omega$ on the sphere.

The procedure described above is then repeated for other momentum intervals and the total polar diagram is obtained by adding up the contributions from the whole spectrum, fig. 7*c*. Now the relative displacement of the polar diagrams corresponding to different momentum intervals puts an upper limit to Δp.

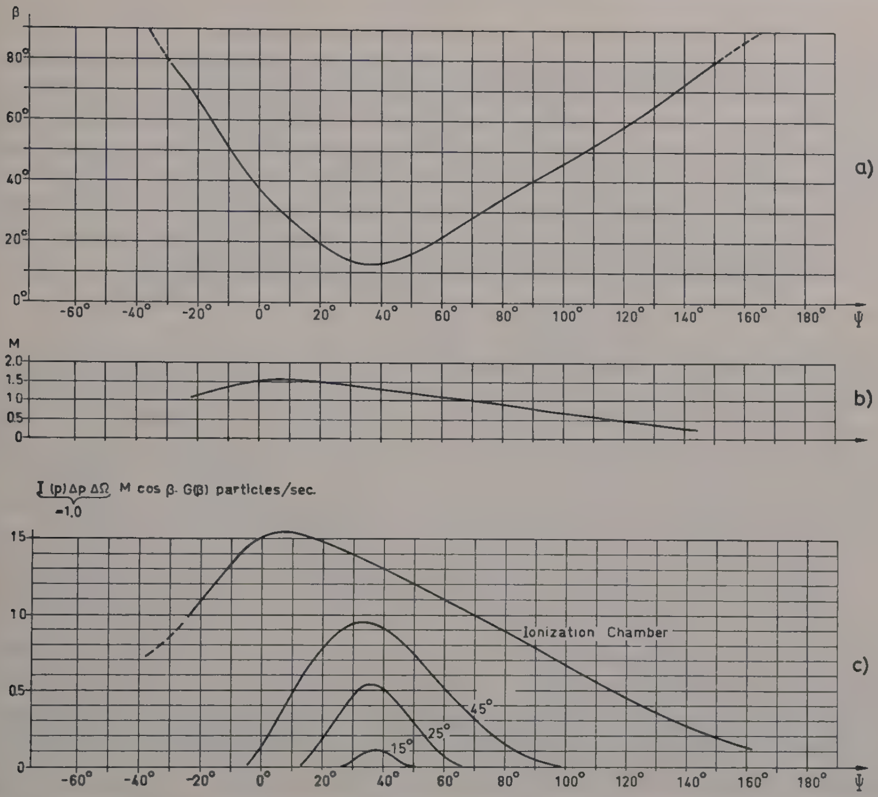

Fig. 8. An example of calculating polar diagrams along $\Phi = 0$ in the momentum range around 50 GeV/c at Huancaoy.

(*a*) The angle of incidence β at the telescope for different angular positions of the source along the equator. (*b*) The magnification M. (*c*) Polar diagrams of zenith pointing telescopes with different apertures, $u_{\max}$.

Fig. 8 illustrates the method of calculating polar diagrams in the momentum interval centred at 50 GeV/c at the Huancayo station (geomagnetic latitude = 0.6° S) with the source element in the equatorial plane ($\Phi = 0$). In fig. 8*a* the zenith angle of incidence, β, at the observation place is plotted. β is found from the Huancayo sphere of asymptotic directions by the different positions Ψ of the source, cf. [15]. Fig. 8*b* shows the corresponding magnification M as a function of Ψ.

The magnification has been approximately determined by projecting the solid angle of a circular telescope with $u_{\max} = 8°$ on the sphere along the equator for different directions of incidence, corresponding to the positions of the source. The ratio $\omega_{8°}/(\omega_{8°})_\infty$ is then taken as representing the magnification M. The accuracy of M when determined in this way is of the order of 0.2–0.3 in the chosen example but for lower momenta the error is considerable and it is finally impossible to determine M. This is due to the fact that the projected solid angles are deformed and their size increased enormously when approaching cut-off momenta. As for each zenith angle only four asymptotic directions are known (N, E, S and W directions) it is thus impossible at present to find the projected solid angles near cut-off momenta on the sphere.

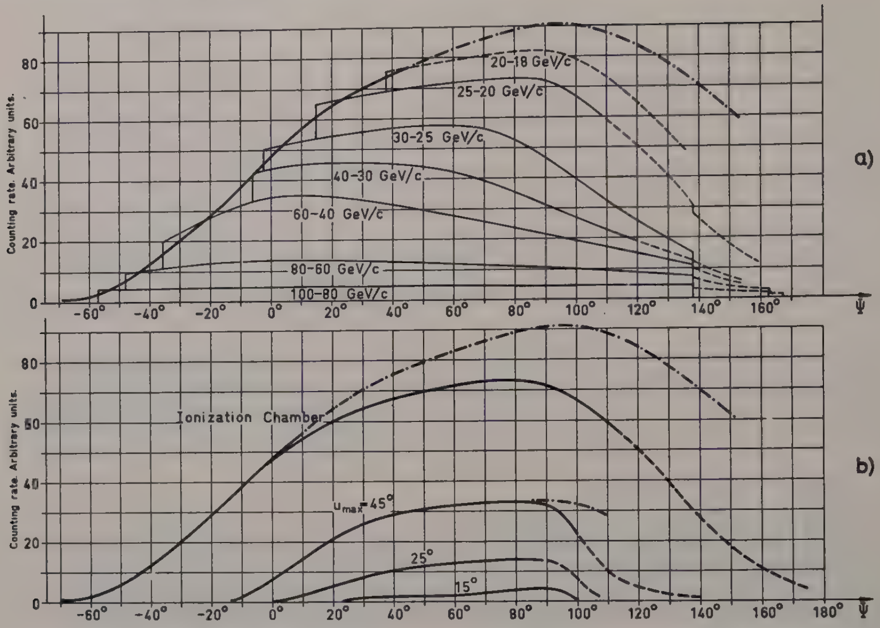

Fig. 9. (*a*) The contributions from different momentum invervals to the polar diagram along $\Phi = 0$ of an ionization chamber in Huancayo. (*b*) Polar diagrams of different telescopes when the primary spectrum in the range 20–100 GeV/c has been used.

Dot-dashed lines represent the probable shape when the contributions from momenta below 20 GeV/c have been included (rough extrapolation). The differential momentum spectrum adopted is proportional to p^{-2}.

Fig. 8*c* shows the polar diagrams obtained with different telescopes using equations 25 and 26 where $I(p)\,\Delta p\,\Delta\Omega$ is for convenience put equal to one.

Fig. 9*a* shows the polar diagram along $\Phi = 0$ of an ionization chamber when the contributions from the primary spectrum in the range 20–100 GeV/c have been added with regard to the proper weights given by the momentum spectrum. The different areas of the polar diagram represent the contributions from different momentum intervals. Dashed lines mean that the values are uncertain which is mainly due to the errors in M as pointed out above. It is seen that the low energy part of the spectrum plays an important role for the shape of the polar diagram. It is consequently necessary to calculate more particle orbits in this region.

In fig. 9*b*, finally, the polar diagrams of cosmic ray telescopes with different apertures are drawn. These diagrams are of great importance for finding the image of a cosmic ray source with the telescope situated above the atmosphere at the Huancayo station. They are discussed further in chapter 3 where the influence of the atmosphere has also been taken into account.

2. THE INFLUENCE OF THE ATMOSPHERE

A cosmic ray telescope at sea level or deep down in the atmosphere records almost only secondary particles produced by nuclear interactions in the atmosphere. The atmospheric influence upon the polar diagram of a telescope is twofold. First the contributions from different parts of the primary momentum spectrum to the polar diagram are not the same as when measuring at the top of the atmosphere, because the production rate and energies of the secondaries are functions of the primary particle energy. Secondly several processes occur in the atmosphere which have a spreading effect upon the secondaries so that a parallel beam of primary particles is gradually converted into a more or less divergent beam of secondaries which are finally recorded by the telescope. This makes the polar diagram wider.

2.1. The spread in the atmosphere

In the beginning of cosmic ray research it was assumed as a first approximation that the direction of particle motion is conserved in the atmosphere. In 1951 Vernov *et al.* [16] deduced experimentally an expression for the angular distribution of secondaries. They found a mean angle of deviation of about 30° between the directions of the secondary and primary particles, i.e. about half the number of the ionizing secondaries are found within a cone with the apex angle 60°. Sandström [17] has pointed out that the spreading effect of the atmosphere should be taken into account when constructing cosmic ray telescopes.

In this chapter the spread of a parallel beam of primary particles is estimated. The different processes occurring in the atmosphere are not completely known; for example the distribution of mesons produced in nucleon-nucleon collisions at different primary energies. In such cases we must make certain assumptions in order to be able to carry the calculations to the final stage and be able to survey the field.

Only the meson component of the secondary flow is considered; that is, we neglect the electron, photon and nucleonic components of the particle flow. Furthermore we assume that the recording apparatus is shielded by 10 cm of lead thus giving response only to μ-mesons of energies higher than 0.1 GeV.

We also assume that a primary particle, after having performed one nuclear interaction with an air nucleon, does not give any further contribution to the μ-meson flow or to the counting rate of a telescope at sea level.

We shall consider three parts of the problem:

(1) The rate of inelastic nucleon-nucleon collisions throughout the whole atmosphere.

(2) The intensity and energy distribution of mesons created in a nucleon-nucleon collision.

(3) Processes influencing the secondaries on their way towards the recording apparatus.

2.1.1. *The rate of inelastic nucleon-nucleon collisions in the atmosphere*

We consider a nearly parallel beam of protons with the energy W_p entering the earth's atmosphere from a direction making the angle β' to the zenith direction, as in fig. 10. The probability of interaction between a primary proton and an air nucleon per unit path length depends on the mass density along the path. If n_0 particles/cm²·sec·sterad. enter the atmosphere in the beam, the number of particles at the height z which have not undergone nuclear interaction is:

$$n_{z\beta'} = n_0 \exp\left(-m_{z\beta'}/L\right). \qquad (27)$$

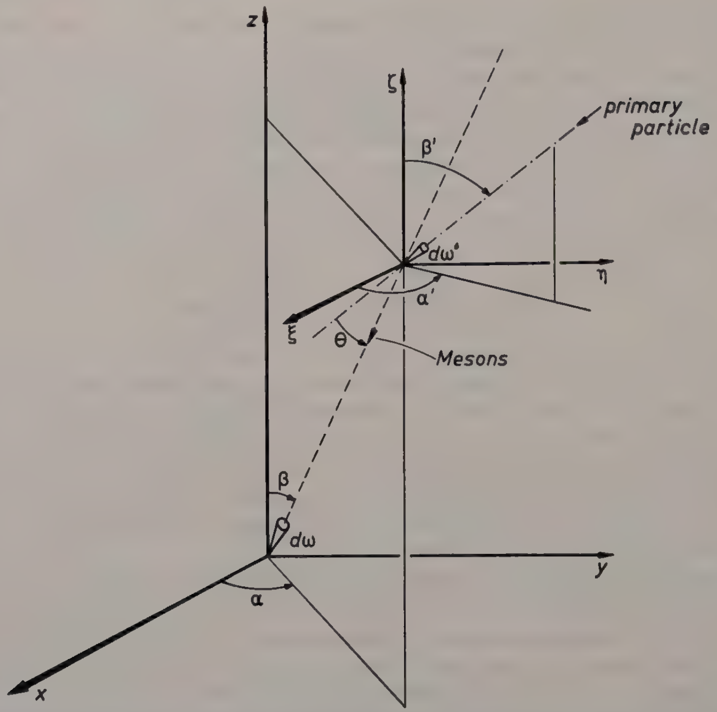

Fig. 10. A telescope at sea level with the infinitely small solid angle $d\omega$ records mesons arriving in the direction α, β. The measons are produced at the height z by primary particles coming from the direction α', β'.

$m_{z\beta'}$ is the penetrated mass of air in g/cm^2 from the top of the atmosphere along a path which makes the angle β' with the vertical. L is the mass corresponding to the mean free path of nuclear interaction for primary particles in air.

Next we want to know the number of particles colliding inelastically, i.e. undergoing nuclear interactions between the heights z and $z + dz$ in the atmosphere which is static and isothermal and thus described by the variation of density:

$$\varrho = \varrho_0 \, e^{-z/l}, \tag{28}$$

where $l = m_0/\varrho_0 =$ the scale height, assumed const.; $m_0 =$ the mass per cm^2 at sea level; $\varrho_0 =$ air density at sea level.

The penetrated mass from the top of the atmosphere to the height z is:

$$m_{z\beta'} = \frac{m_0}{\cos\beta'} \, e^{-z/l}. \tag{29}$$

The number of inelastic collisions between the heights z and $z + dz$ is from equations 27 and 29 by derivation:

$$dn_{z\beta'} = n_0 \frac{m_0}{L l \cos\beta'} \exp\left[-\frac{z}{l} - \frac{m_0}{L\cos\beta'} \exp\left(-\frac{z}{l}\right)\right] dz \quad \text{particles/cm}^2 \cdot \text{sec} \cdot \text{sterad.} \tag{30}$$

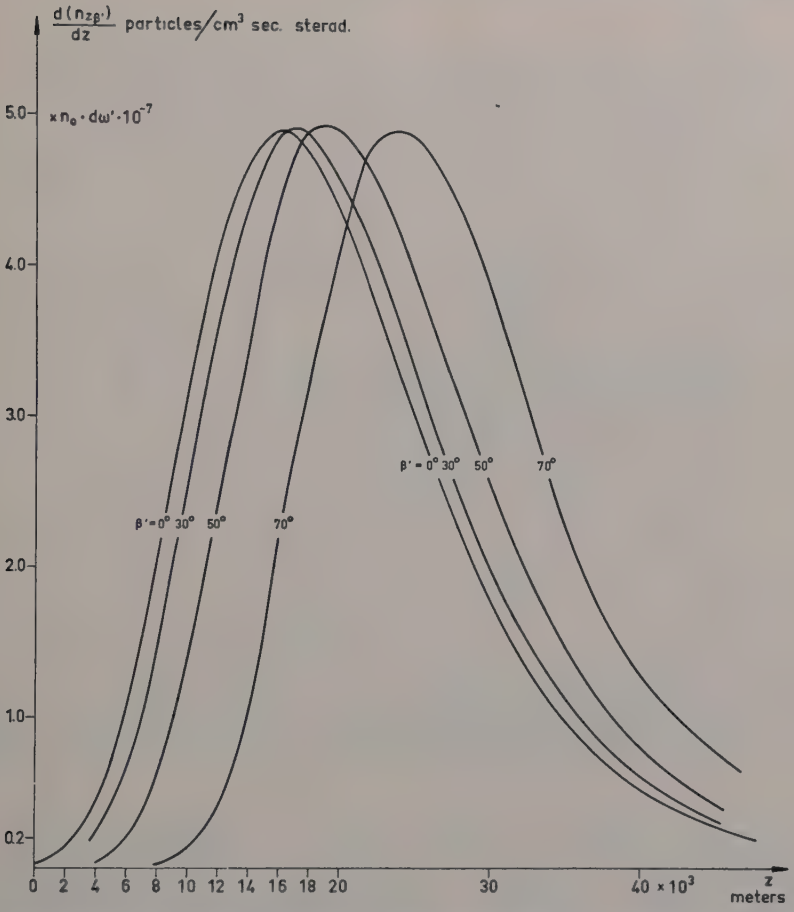

Fig. 11. The number of inelastic collisions in the atmosphere as a function of the height for different angles of incidence to the vertical.

$dn_{z\beta'}$ is consequently the change in the number of primary particles of the beam which have not undergone nuclear interaction, in a layer dz of the atmosphere.(¹)

The number of inelastic collisions per unit volume is (from eq. 30):

$$\frac{dn_{z\beta'}}{dz} = n_0 \frac{m_0}{L\,l\cos\beta'} \exp\left[-\frac{z}{l} - \frac{m_0}{L\cos\beta'} \exp\left(-\frac{z}{l}\right)\right] \quad \text{particles/cm}^3 \cdot \text{sec} \cdot \text{sterad.} \qquad (31)$$

The number of inelastic collisions per unit volume according to eq. 31 has been plotted in fig. 11 as a function of the altitude for different values of β' and with

---

(¹) The atmospheric depth in g/cm² taken from the top of the atmosphere is often used in expressions of this type instead of the height z above sea level. As we are interested in knowing where the production rate of secondaries is a maximum we are forced to introduce the mass distribution of the atmosphere. Furthermore, the path length of secondaries enters into the calculations, which is another reason for using the height z in the present equations.

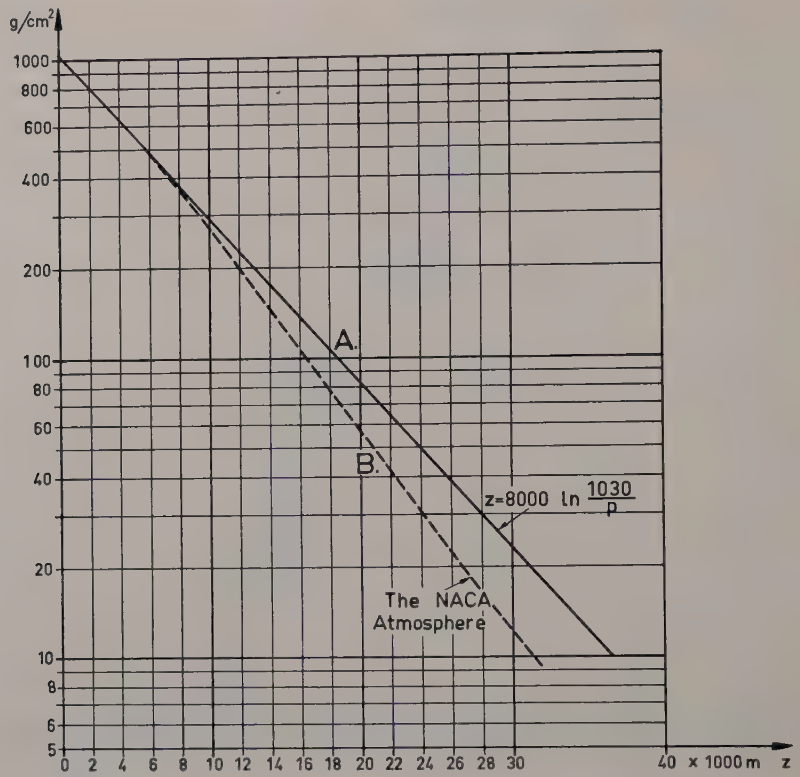

Fig. 12. The mass distribution in the atmosphere.

$m_0 = 1030$ g/cm² and 1 = 8000 m. L probably depends little on the primary energy and experiments give values between 100–150 g/cm² (compare Rossi [18, p. 442], and Sands [19]). The value 120 g/cm² has been used in the present calculations.

We define the production rate of secondaries as the product of the number of nuclear interactions and the average number of mesons produced per interaction.

The maximum production rate for primary particles arriving in the zenith direction occurs at a height of 17 km, as seen from fig. 11. This corresponds to a pressure of 120 g/cm² with the assumed atmosphere or to 90 g/cm² using the "NACA-atmosphere" (National Advisory Committee for Aeronautics), fig. 12.

The number of inelastic collisions per unit volume, integrated over all primary directions, assuming isotropic distribution of particles over the hemisphere and above the atmosphere, is:

$$\frac{dn}{dz} = \int\limits_{\alpha'=0}^{2\pi} \int\limits_{\beta'=0}^{\pi/2} \frac{n_0 m_0}{L\, l \cos\beta'} \exp\left[-\frac{z}{l} - \frac{m_0}{L\cos\beta'} \exp\left(-\frac{z}{l}\right)\right] \sin\beta'\, d\beta'\, d\alpha' \quad \text{particles/cm}^3 \cdot \text{sec} \qquad (32)$$

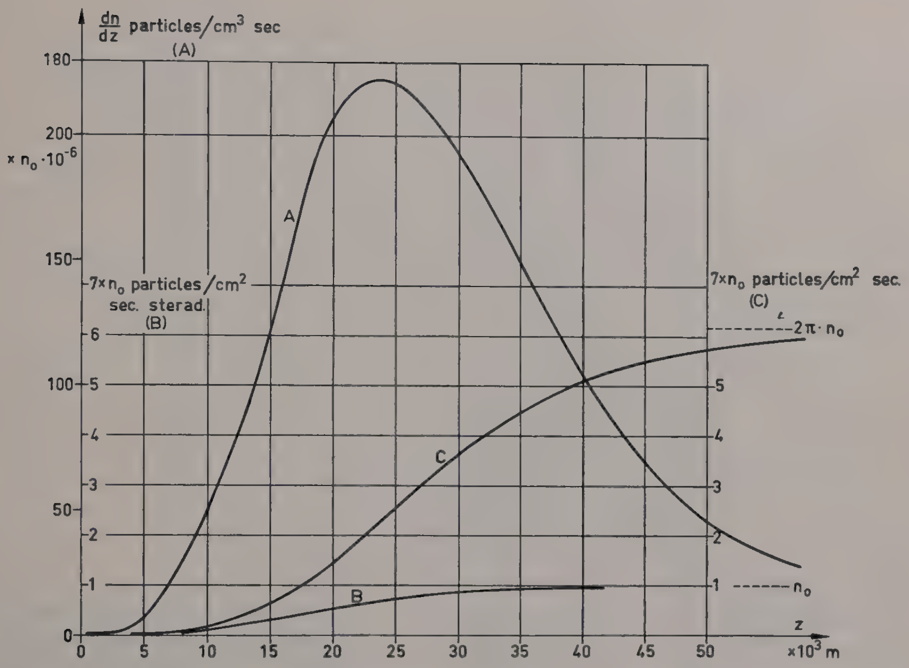

Fig. 13. *Curve A:* The total number of inelastic collisions per unit volume in the atmosphere as a function of the height. *Curve B:* The number of primary particles from the zenith direction which have not collided inelastically. *Curve C:* The total number of primary particles which have not collided inelastically (particles/cm² · sec).

where α' is the azimuth angle of the primary beam, as in fig. 10. The integration has been carried out in appendix II and the total number of inelastic collisions per unit volume plotted in fig. 13. The maximum total production rate according to these calculations occurs at a height of around 24 km, which corresponds to a pressure of 30 g/cm² in the NACA-atmosphere.

Measurements of the ionization in the atmosphere with balloons and rockets using unshielded ionization chambers show a maximum at a pressure between 40–110 g/cm², depending on the geomagnetic latitude λ. The lower value is at $\lambda = 60°$ N and the high one near the equator according to Bowen, Millikan and Neher [20], Gangnes *et al.* [21].

The vertical intensity measured by Vidale [22] has a maximum at 75 g/cm² ($\lambda = 55°$) and 135 g/cm² ($\lambda = 28°$) for the total radiation, whereas the corresponding figures for the hard component are approximately 48 and 120 g/cm². The maximum ionization is thus measured lower down in the atmosphere compared to the level of the maximum production rate (30 g/cm²) found in our calculations.

This is however what would be expected since an instrument records not only secondaries produced near it but also secondaries coming from higher up in the atmosphere as well as the primary particle intensity itself. If all secondaries could reach sea level the intensity would obviously increase with decreasing altitude and highest intensity be measured at sea level. If, on the other hand, the number of secondaries produced at a certain altitude were to decrease with a very short mean free path,

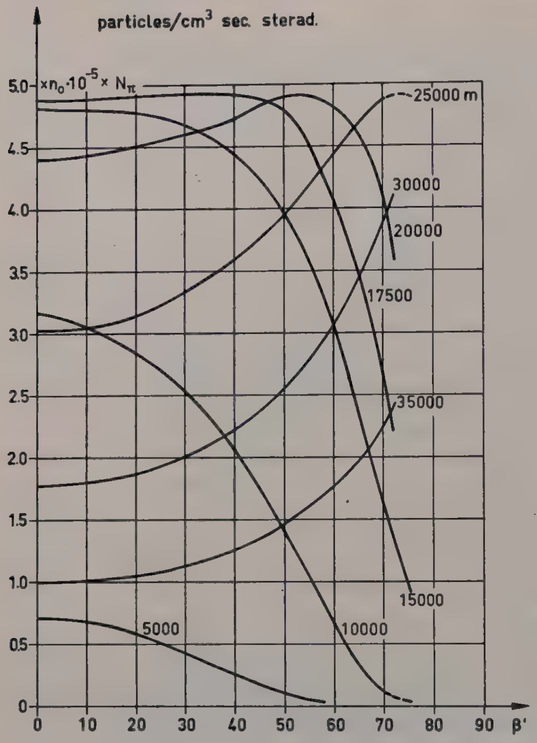

Fig. 14. The production rate at different altitudes as a function of the zenith angle of incidence β'. N_π is the average number of mesons produced in a nucleon-nucleon collision.

maximum intensity would be measured near the level where the production rate is maximum. In reality there is a decrease in intensity due to absorption and decay which shifts the maximum towards lower altitudes.(¹)

The observed latitude dependence of the height of maximal ionization is probably due to the lower mean energy of secondaries which are produced by the low energy part of the primary spectrum. As these secondaries decay more rapidly and are absorbed after a shorter path length the maximum ionization should be measured nearer to the level of maximum production, which according to our calculations is at 30 g/cm². The measured shift of the level of maximum ionization from 110–130 g/cm² at lower latitudes up to 40–80 g/cm² at high latitudes, where there are more primaries of low energy, is in qualitative agreement with the hypotheses of a height difference between the levels of maximum production rate and maximum ionization.

When discussing the production rate in the atmosphere it should be pointed out that the zenith angle dependence of the intensity at different altitudes is probably explained by the number of inelastic collisions per unit volume given by eq. 31 or properly speaking by the production rate. Different authors have found that the intensity increases with zenith angle above a certain altitude (Winckler and Stroud

---

(¹) For example the decay of μ-mesons with energy W_μ is given by:

$$n_\mu = n_{0\mu} \exp(-s/c\tau),$$

where s = the path length; $\tau = \tau' \, (W_\mu/m_\mu c^2)$; and τ' is the decay time of a μ-meson at rest. With $W_\mu = 1$ GeV the mean free path of decay is 6000 m.

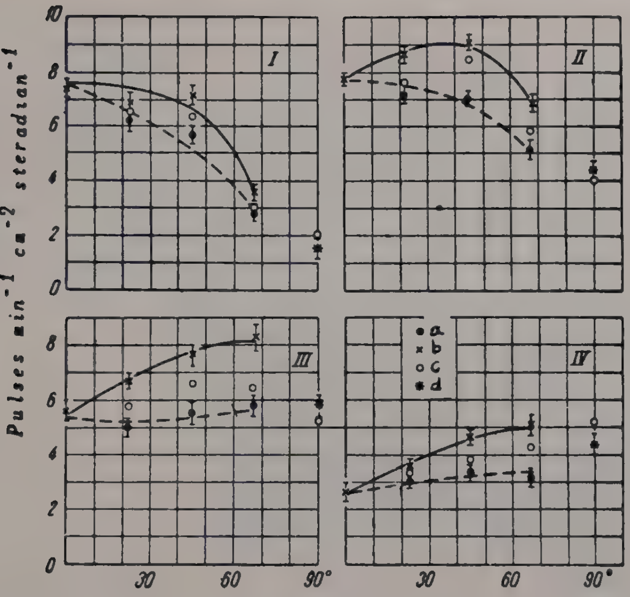

Fig. 15. Zenithal and azimuthal distribution of cosmic ray intensity at the equator (Vernov *et al.*).

I.	10 km	*a.*	East
II.	15	*b.*	West
III.	21	*c.*	North or South
IV.	26	*d.*	West–East

[23], Vernov *et al.* [24]). It has been suggested by Singer [25] that this is due to an albedo effect.

Winckler and Stroud, however, have compared the measurements of the zenithal particle distribution with their own calculations of the expected distribution, assuming different absorption coefficients for the primary and secondary particles. They have investigated the influence of different angular distributions of secondaries and have found that the closest agreement is reached by assuming a sharply collimated forward type of distribution.

From eq. 31 the number of inelastic collisions per unit volume in the atmosphere has been calculated as a function of the zenith angle β' with the height to the production level as a parameter. This has been plotted in fig. 14. Assuming as a first approximation that all the mesons produced in nucleon-nucleon collisions move in the same direction as the arriving protons, fig. 14 gives the production rate of secondaries in different directions in the atmosphere. We notice that up to about 15000 m the production rate is a decreasing function of β', at 17000 m it is constant for $\beta' < 45°$ and above 20000 m it increases with the zenith angle.

Allowing for a shift towards lower altitudes according to what was discussed above these curves are in good agreement with the measurements of Vernov *et al.* and Winckler and Stroud (compare figs. 14, 15 and 16). We thus conclude that eq. 32 and figs. 12, 13 and 14 are representative of the production rate in the atmosphere.

Finally, assuming isotropic particle distribution over the hemisphere above the

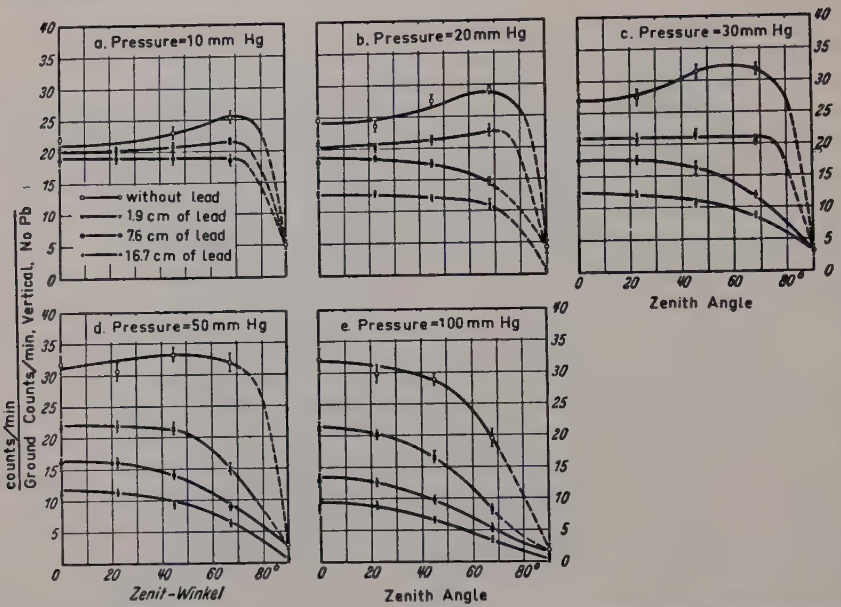

Fig. 16. The zenithal distribution of cosmic ray intensity measured at 56° geomagnetic latitude (Winckler and Stroud).

atmosphere, the zenith angle dependence of the intensity at sea level could be derived by superimposing the curves of fig. 14, with the decay and absorption of μ-mesons taken into consideration. This means that the contribution from different levels decreases with increasing height. A calculation along these lines is carried out in section 2.3.

2.1.2. *The intensity and energy distribution of mesons produced in nucleon-nucleon collisions*

The interaction between a primary cosmic ray particle and an air nucleon results in the production of secondary particles, as for example other nucleons, electrons and different kinds of mesons. For the primary energies which are most interesting in our problem the production of π-mesons is important. We want to know the intensity and energy distribution of the produced π-mesons as function of the angle between the direction of the arriving primary particle and the direction of the emitted mesons in a coordinate system at rest (L-system).

This is done firstly by finding the intensity and energy distribution of the mesons in the centre of mass system of the two colliding nucleons (C-system). Secondly, these distributions are transformed to the L-system.

The intensity distribution of the produced mesons in the C-system is probably anisotropic at high primary energies, as pointed out by Schein *et al.* [26], but in the range around 10 GeV the distribution is more likely to be isotropic. This is assumed in the following calculations in the absence of more precise information [27, 28].

The energy distribution of π-mesons in the C-system has been studied by Camerini *et al.* [29]. Under the assumption that all the mesons are produced in a single nucleon-

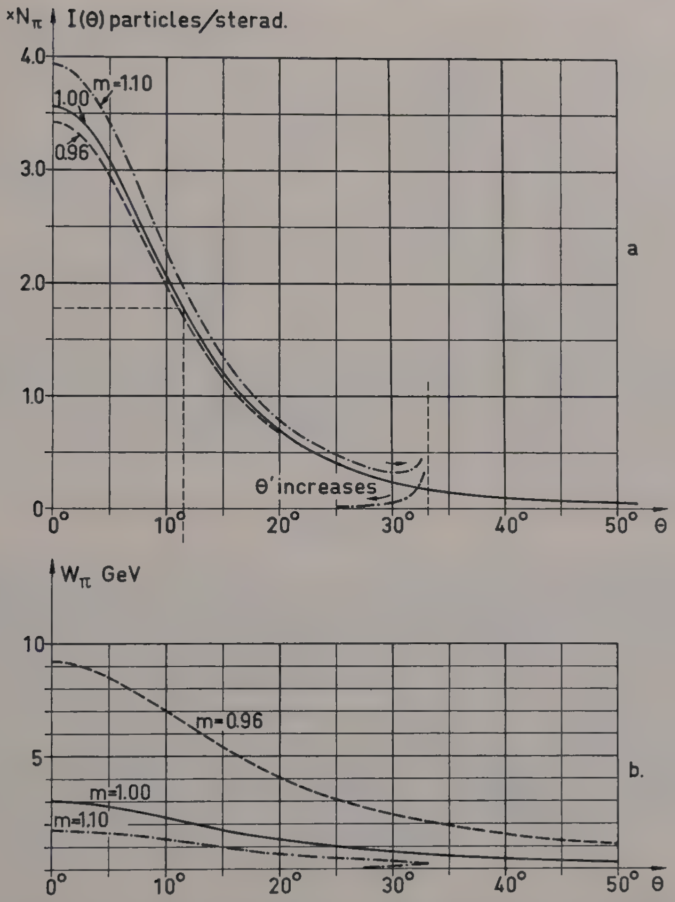

Fig. 17. (*a*) The angular intensity distribution of π-mesons in the L-system. Each curve corresponds to π-mesons produced isotropically in the C-system all with the same energy. In the energy case corresponding to $m = 1.10$ there are no mesons in the L-system for $\theta > 33°$. This is explained by Bradt, Kaplan and Peters [30]. (*b*) The angular energy distribution of π-mesons in the L-system.

nucleon collision these authors find a differential spectrum which is approximately represented by:

$$\frac{dn_\pi}{d\gamma'_\pi}=\frac{\sqrt{(\gamma'_\pi)^2-1}}{(\gamma'_\pi)^3}, \tag{33}$$

where γ'_π is the energy of a π-meson in C-system in terms of its rest energy.

The transformation of the intensity and energy distributions to the L-system has been treated in great detail by Bradt, Kaplan and Peters [30]. The complete formulae for the angular intensity distribution $I(\theta, W_p)$ and the π-meson energy expressed in units of the rest energy $\gamma_\pi(\theta, W_p)$ in the L-system are collected in appendix III.

The shape of the distribution function $I(\theta, W_p)$ in the L-system is determined mainly by the primary proton energy W_p but also by m, i.e. the ratio between the proton and meson velocities in the C-system. The value of meson velocity v'_π in the C-system is dependent on the inelasticity of the collision (i.e. the ratio between the energy of the produced mesons and the total energy available) and the total multiplicity which includes both charged and uncharged π-mesons.

The following calculations have been carried out for 20 GeV/c protons as an example, because this momentum seems to be representative of the primary spectrum when measuring the position of the cosmic ray source, which is responsible for the daily variation of cosmic ray intensity (Brunberg and Dattner [31]).

The Camerini-distribution (eq. 33) has been approximated by a step function by choosing three energy intervals in such a way that the same number of mesons are contained in each energy interval. The mean meson energy of each interval, together with assumed primary energy W_p, yields the values of $m = 1.10$, 1.00 and 0.96 with the corresponding values of $\gamma'_\pi = 2.0$, 3.35 and 10.0. For these values the distributions of intensity and kinetic energy of π-mesons in the L-system have been calculated using the formulae of appendix III. The results are shown in fig. 17.

2.1.3. *Different processes influencing the intensity and energy distributions of mesons*

On their way down through the atmosphere the charged μ-mesons interact with air nuclei or decay into μ-mesons and neutrinos. The number of μ-mesons then decreases gradually due to absorption and decay. Finally, Coulomb-scattering and deflection in the earth's magnetic field have a spreading effect on the μ-meson beam.

2.1.3.1. *The $\pi \rightarrow \mu$ decay*

The mean life of a π-meson before it decays into a μ-meson and a neutrino is about 2.5×10^{-8} s. The mean free path is calculated from :

$$l_\pi = \frac{c\,\tau'\,W_\pi}{m_\pi\,c^2}, \tag{34}$$

where τ' is the decay time in the system at rest.

With $W_\pi = 3$ GeV we get $l_\pi = 160$ m which is negligible in the calculations.

The decay of the π-mesons introduces a small spreading effect, so that the μ-meson beam is slightly more divergent than the original π-meson beam. The magnitude of this effect is estimated by calculating the angular half-width $\theta_{\frac{1}{2}}$ in the L-system of the μ-meson intensity distribution. The angular half-width $\theta_{\frac{1}{2}}$ is defined by a cone with the apex angle $2\theta_{\frac{1}{2}}$ within which half the number of the produced μ-mesons is found in the L-system. We use the modified eq. AIII.3 in appendix III:

$$\operatorname{tg}\theta = \frac{\sin\theta'}{\cos\theta' + v_\pi/v'_\mu}\sqrt{1-\left(\frac{v_\pi}{c}\right)^2}. \tag{35}$$

As, in the C-system (the moving π-meson), any direction is equally probable for the created μ-meson, the distribution in the C-system of a large number of events is isotropic. The half-width in the L-system is thus obtained by putting $\theta' = \frac{1}{2}\pi$ in eq. 35:

$$\operatorname{tg}\theta_{\frac{1}{2}} = \frac{v'_\mu}{v_\pi}\sqrt{1-\left(\frac{v_\pi}{c}\right)^2}. \tag{36}$$

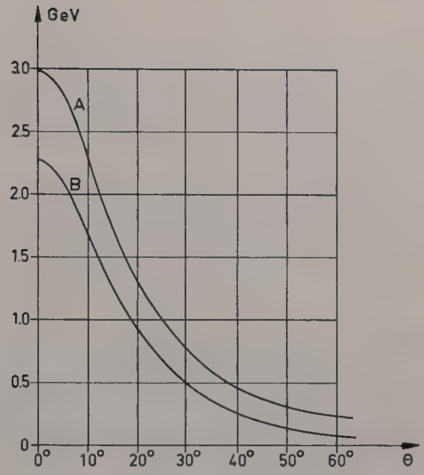

Fig. 18. The angular energy distribution of mesons in the L-system for $m = 1$. *Curve A:* The total energy of π-mesons. *Curve B:* The mean kinetic energy of μ-mesons due to the $\pi \rightarrow \mu$ decay.

Using the formulae for particle decay to determine the momentum $p'_\mu \approx 30$ MeV (cf. Heisenberg [7], p. 561) and 3 GeV as the π-meson energy as an example, the half-angle amounts to 0.9° which is quite negligible compared to the half-angle of the intensity distribution of π-mesons which, with eq. AIII.19 in appendix III, is found to be 18° for 20 GeV/c primary protons.

The energy distribution is, however, modified by the decay. π-mesons of energy W_π, emitted at an angle θ to the direction of the primary beam, form a spectrum of μ-mesons of energies ranging from a maximum to a minimum value and with a small spread in angle as discussed above. This narrow interval can be looked upon as a compressed strip at the angle θ containing all energies between the maximum and minimum values, as pointed out by Ascoli [32].

The μ-meson energy is given there by:

$$W_\mu = \tfrac{1}{2}\left[\frac{m_\pi}{m_\mu} + \frac{m_\mu}{m_\pi}\right]\frac{m_\mu c^2}{m_\pi c^2}\, W_\pi \pm \frac{p_\pi}{m_\pi}\, p'_\mu \cos\theta' \tag{37}$$

or

$$W_\mu = 0.789\, W_\pi \pm c p'_\mu \sqrt{\gamma_\pi^2 - 1} \times \cos\, \theta', \tag{38}$$

where p'_μ is the momentum of the μ-meson in the C-system due to the decay.

With $W_\pi = 3.0$ GeV eq. 38 is written:

$$W_\mu = 2.36 + 0.63 \times \cos\theta' \text{ GeV}. \tag{39}$$

As any energy in the interval between $(W_\mu)_{\max}$ and $(W_\mu)_{\min}$ is equally probable we give each meson the mean value:

$$\langle W\mu\rangle = 0.789\, W_\pi. \tag{40}$$

The angular distribution of kinetic energy of the μ-mesons is calculated in this way and plotted in fig. 18.

2.1.3.2. *The decay and absorption of μ-mesons*

As shown in the previous section, the angular distribution of meson intensity remains practically unchanged by the $\pi \rightarrow \mu$ decay.

The angular distribution of μ-mesons originating from a thin atmospheric layer dz at the height z is, according to eq. 31 in section 2.1.1.:

$$dn_{\mu z} = I(\theta, W_p) \frac{n_0 m_0}{L l \cos\beta'} \exp\left[-\frac{z}{l} - \frac{m_0}{L\cos\beta'} \exp\left(-\frac{z}{l}\right)\right] dz\, d\omega' \quad \text{particles/cm}^2 \cdot \text{sec} \cdot \text{sterad.,} \qquad (41)$$

where $d\omega'$ is the solid angle subtended by the primary cosmic ray beam and $I(\theta, W_p)$ the angular intensity distribution of produced mesons in a nucleon-nucleon collision.

If the μ-mesons were to travel without losses or any other disturbing effects, a telescope with the surface da and an infinitely narrow solid angle $d\omega$ perpendicular to the surface would record:

$$d^3 n_\mu = da\, d\omega\, dn_{\mu z} \quad \text{particles/sec.} \qquad (42)$$

Due to decay, the particle density of the μ-meson beam decreases and a telescope at sea level measures:

$$d^3 n_\mu = da\, d\omega\, dn_{\mu z} \exp\left(-\frac{z}{v_\mu \tau \cos\beta}\right) \quad \text{particles/sec.,} \qquad (43)$$

where $\tau = \tau'(W_\mu / m_\mu c^2)$ and $v_\mu =$ the velocity of the μ-meson which is approximately equal to that of light.

Introducing the numerical values: $\tau' = 2.15 \times 10^{-6}$ sec., $m_\mu c^2 = 0.107$ GeV, $v_\mu = 3 \times 10^8$ m/s, eq. 43 is written:

$$d^3 n_\mu = da\, d\omega\, dn_{\mu z} \exp\left(-\frac{z}{C_1 W_\mu \cos\beta}\right), \qquad (44)$$

where $C_1 = 60.3 \times 10^2$ if W_μ is expressed in units of 10^9 volts. The change of W_μ along the path, due to atmospheric losses, modifies the distribution given by eq. 44 but this effect is found to be negligible.

The μ-mesons lose energy through ionization and excitation in the atmosphere. The magnitude of the energy loss depends on the μ-meson energy and the penetrated mass and is found, for example, in Heisenberg, *Kosmische Strahlung*, p. 577. The losses are approximately independent of energy in the actual energy range from 0.1 GeV and upwards with:

$$\frac{dW}{dm} \approx 2 \times 10^{-3} \frac{\text{GeV}}{\text{g/cm}^2}. \qquad (45)$$

The penetrated mass Δm between the height of meson production z and a telescope at sea level is:

$$\Delta m = \frac{m_0}{\cos\beta}\left[1 - \exp\left(-\frac{z}{l}\right)\right] \text{g/cm}^2 \qquad (46)$$

and the loss of μ-meson energy consequently:

$$\Delta W_{\mu} = \frac{d W}{d m} \frac{m_0}{\cos \beta} \left[1 - \exp \left(- \frac{z}{l} \right) \right] \text{ GeV.} \tag{47}$$

A telescope records mesons coming from a given height z if the initial kinetic meson energy is larger than the total energy loss, which includes losses both in the atmosphere and in the recording apparatus. Thus, all mesons of the given energy are either recorded by the telescope or not depending on the angle of incidence β. This is allowed for by introducing a function $J(z, \beta, W_{\mu \,\mathrm{kin}})$, defined by:

$$J = 1 \text{ when } W_{\mu \,\mathrm{kin}} > \Delta W_{\mu} + \Delta W_a \quad \text{GeV} \tag{48a}$$

$$J = 0 \text{ when } W_{\mu \,\mathrm{kin}} < \Delta W_{\mu} + \Delta W_a \quad \text{GeV} \tag{48b}$$

$W_{\mu \,\mathrm{kin}}$ is the initial energy of a μ-meson starting towards the telescope, ΔW_{μ} is given by eq. 47 and ΔW_a is the energy loss in the recording apparatus (0.1 GeV assumed).

Summary.—The complete expression for the counting rate of a telescope, situated at sea level and pointing in a direction making the angle β with the vertical, is given by eq. 49 a, when the telescope records μ-mesons which are produced at the height z in the interval dz. The telescope has an infinitely small solid angle $d\omega$ and its infinitely small surface da is perpendicular to the direction of $d\omega$:

$$d^4 n_{\mu} = da\, d\omega\, I(\theta, W_p) \underbrace{\frac{m_0}{L\, l \cos \beta'} \exp \left[- \frac{z}{l} - \frac{m_0}{L\, l \cos \beta'} \exp \left(- \frac{z}{l} \right) \right]}_{R} \times$$

$$\times \underbrace{\exp \left[- \frac{z}{C_1 W_{\mu} \cos \beta} \right]}_{D} J\, dz\, n_0\, d\omega'. \tag{49a}$$

$I(\theta, W_p)$ describes the angular intensity distribution of mesons at the production level z. R gives the production rate at this level for a primary beam of particles subtending the solid angle $d\omega'$ and coming from a direction defined by the angles α' and β' (fig. 10). D represents the decrease in meson intensity due to decay, and J represents the absorption. The product of the functions $I(\theta, W_p)$, R, J, and D is denoted $K(\theta, W_p, z)$ in the following. Thus:

$$d^4 n_{\mu} = da\, d\omega\, K(\theta, W_p, z)\, dz\, n_0\, d\omega'. \tag{49b}$$

The relation between the measuring direction of the telescope $(\alpha . \beta)$, the direction of the primary beam $(\alpha' \beta')$ and θ is found from fig. 10 and given by:

$$\cos \theta = \sin \beta \sin \beta' \cos(\alpha - \alpha') + \cos \beta \cos \beta'. \tag{50}$$

The effect of decay and absorption is that the intensity distribution measured deep down in the atmosphere has a sharper maximum than that measured just

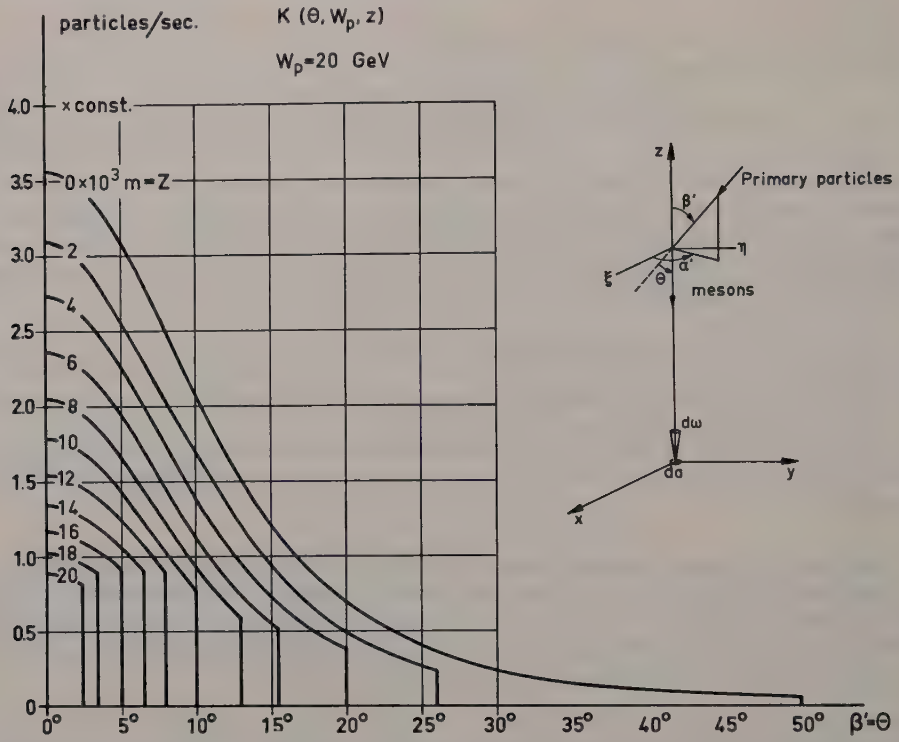

Fig. 19. The contributions of different production levels to the counting rate of a zenith pointing telescope with infinitely small solid angle $d\omega$. The curves correspond to the π-meson energy $\gamma'_\pi = 3.35$ in the C-system, which corresponds to $m = 1.00$.

below the level of production. This is due to the energy distribution of the μ-mesons. Mesons starting in a direction making a large angle θ with the primary beam have smaller energies and will consequently decay more rapidly, seen from the laboratory system, than those starting in directions which differ little from the primary direction. Furthermore, they are absorbed after a shorter path length than mesons of higher energies.

In fig. 19 we have plotted the counting rate of a zenith pointing telescope with the surface da and solid angle $d\omega$ for different production levels as a function of the angle β' of the incident primary beam. β' equals θ in this case. The different curves represent the counting rate of the telescope for different production levels. Here it is assumed that the production rate is the same for all levels. The uppermost curve is proportional to the function $I(\theta, W_p)$ and corresponds to production at sea level. With increasing height to the meson producing layer the counting rate is reduced by the decay and at a certain angle there is a cut-off when the absorption limit is reached. The curves in fig. 19 are calculated for the case $m = 1.00$ which corresponds to a π-meson energy of 3 GeV (giving a mean kinetic energy of 2.3 GeV to the μ-meson) in the forward direction in the L-system (see fig. 18).

The total counting rate for any β'-value is obtained by adding the contributions

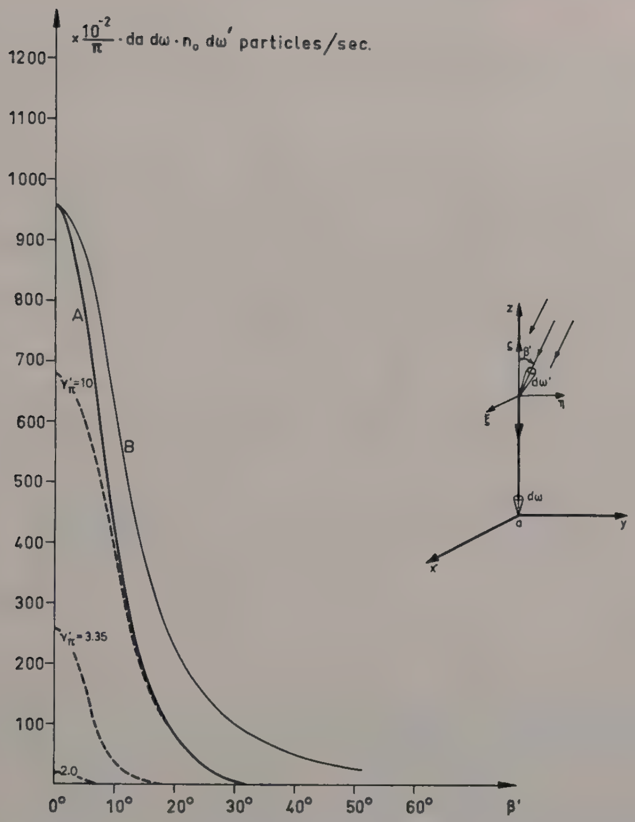

Fig. 20. Dashed curves: The counting rate of a zenith pointing telescope as a function of β', the zenith angle of incidence of the primary beam. The curves correspond to three different π-meson energies in the C-system.

A, The sum of the three curves (i.e. the image when geomagnetic deflection is not taken into account). B, The normalized intensity distribution $I(\theta, W_p)$ just below the point of a nucleon-nucleon collision.

from all production layers, i.e. by adding the curves of fig. 19, each of them with a weight given by the production rate at the corresponding height and by the angle β', as in fig. 11.

The same calculations have been repeated for the π-meson energies $\gamma'_\pi = 10.00$ and 2.00 and the three distributons have then been added with the same weight, according to section 2.1.2.

The result is shown in fig. 20. We notice that the width of the resulting distribution is decreased by the influence of the atmosphere and the decay.

2.1.3.3. *Scattering of μ-mesons*

The mesons are scattered by elastic collisions in the atmosphere. The multiple scattering is described by the mean square angle of scattering $\langle \theta^2 \rangle$ which is obtained by using the Rutherford scattering formulae; cf. Rossi [18, p. 66]:

$$\langle \theta^2 \rangle = \frac{W_s^2}{c^2} \cdot \frac{1}{X_0} \int_{p_1}^{p_2} \frac{1}{\beta^2 (-dp/dx)} \cdot \frac{dp}{p^2}, \tag{51}$$

where p_1 = momentum of a particle at the apparatus, p_2 = momentum of a particle at the production level. $W_s = 21 \times 10^9$ eV and X_0 is a constant of the penetrated matter which equals 38 g/cm² for air. dp/dx is the momentum loss per unit of penetrated mass and β is the particle velocity in units of the velocity of light, c.

We express eq. 51 in terms of energy because the previous calculations have been performed in terms of energy. By using equations 52 and 53:

$$c^2 p^2 = W_{\text{kin}}^2 + 2\, W_{\text{kin}}\, W_0, \tag{52}$$

$$W_{\text{kin}} + W_0 = m c^2, \tag{53}$$

where W_{kin} = kinetic energy of a particle and W_0 its rest energy, we get:

$$\langle \theta^2 \rangle = \frac{W_s}{X_0} \cdot \frac{1}{(-dp/dx)} \int_{W_{1\text{kin}}}^{W_{2\text{kin}}} \frac{(W_{\text{kin}} + W_0)^2}{[(W_{\text{kin}} + W_0)^2 - W_0^2]}\, d W_{\text{kin}}. \tag{54}$$

dp/dx has been taken as a constant in the momentum range considered.

The solution is:

$$\langle \theta^2 \rangle = \frac{W_s^2}{X_0} \cdot \frac{1}{(-d\, W_{\text{kin}}/dx)} \Bigg/_{W_{2\text{kin}}}^{W_{1\text{kin}}} \left\{ \frac{W_{\text{kin}} + W_0}{2\,[(W_{\text{kin}} + W_0)^2 - W_0^2]} + \frac{1}{4\, W_0} \ln \left(\frac{2\, W_0 + W_{\text{kin}}}{W_{\text{kin}}} \right) \right\}. \tag{55}$$

$\sqrt{\langle \theta^2 \rangle}$ has been calculated for different values of $W_{1\text{kin}}$ and $W_{2\text{kin}}$ and the result plotted in fig. 21 with $(-d\, W_{\text{kin}}/dx) = 2$ MeV/cm.

Rossi [18, p. 69] has discussed the scattering of a parallel and infinitely thin beam of particles, all of the same energy, which enters a scattering substance.

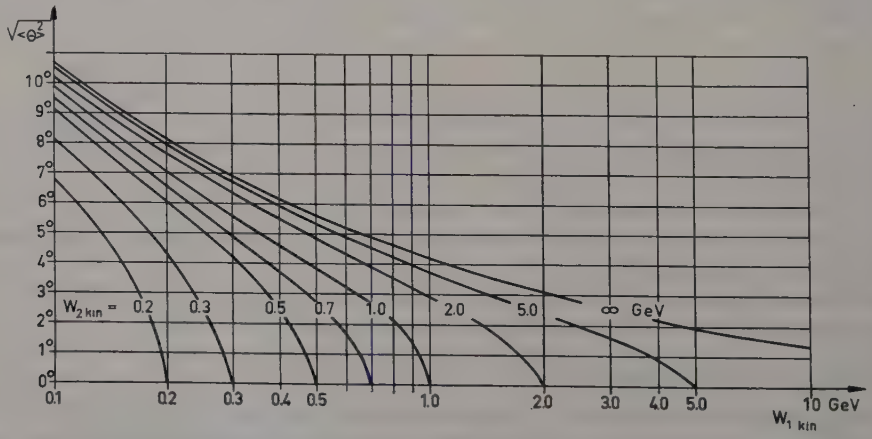

Fig. 21. The mean square angle of scattering in air for μ-mesons of different energies. $W_{2\text{ kin}}$ and $W_{1\text{ kin}}$ are the energies at the beginning and the end of the path respectively.

Let the direction of the incident beam be along the z-axis in a system of cartesian coordinates. The angular distribution of particles, irrespective of lateral displacement, is then represented by:

$$Q(z, \vartheta_y) = \frac{1}{\sqrt{\pi \langle\theta^2\rangle}} \exp\left(-\frac{\vartheta_y^2}{\langle\theta^2\rangle}\right). \tag{56}$$

Eq 56 gives the number of particles with directions of motion between ϑ_y and $\vartheta_y + d\vartheta_y$ taken over all values of the lateral displacement y. ϑ_y is the projection of the scattering angle in the $z-y$ plane.

For a parallel beam of infinite extension in both x- and y-directions (which is the case in the present calculations) eq. 56 gives the angular distribution at any point and is used in the following when estimating the angular spread of the μ-meson beam.

This could be done thoroughly by calculating the scattering of mesons which originate from different production levels and directions and thus finding the resulting angular distribution of μ-mesons at sea level.

However, it is enough for our purpose to show that the influence of the scattering can be neglected in the present calculations.

The angular distribution at each production level, the function $I(\theta, W_p)$, can be represented by a Gauss distribution:

$$I(\theta, W_p) \approx A \exp(-\theta^2/\theta_0^2),$$

where θ_0 is found to be about 16° (Curve B in fig. 20). If we consider the energy case $\gamma'_\pi = 3.35$, the mean kinetic energy of the produced μ-mesons is given by curve B in fig. 18. The contributions from different production levels to the counting rate at sea level come from heights up to 20000 m, as seen from fig. 19. The production rate increases approximately linearly with the height, see fig. 11. We thus take the production level 12000 m as representative of the whole range of production levels. The energy loss ΔW_μ in the atmosphere is about 1.7 GeV for μ-mesons coming from this height in the vertical direction. From figs. 18 and 21 it is found that $\sqrt{\langle\theta^2\rangle}$ varies between 4° and 10° where the high value is at the absorption limit. If we take the scattering to be constant over the whole region and equal to 10°, the original distribution is widened and the new distribution described by $\theta_{0s} = \sqrt{10^2 + 16^2} = 19°$. Thus, the broadening of the distribution is certainly less than 3° in the energy case $\gamma'_\pi = 3.35$. The resulting distribution when adding the three distributions corresponding to $\gamma'_\pi = 2.0$, 3.35 and 10.00 is influenced still less, as the scattering in the energy case $\gamma'_\pi = 10.00$ is much less due to the higher μ-meson energies. The contribution in the energy case $\gamma'_\pi = 2.0$ is negligible.

We thus conclude that the influence of the Coulomb scattering can be neglected in the present calculations compared with other approximations.

2.1.3.4. *Magnetic deflection of the μ-mesons in the atmosphere*

The mesons are deflected in the earth's local magnetic field between the production level and the telescope. The magnitude of the deflection depends on the meson energy, the measuring direction of the telescope and the magnetic field at the place of observation. At the equator where the magnetic field is about 0.3 gauss the total deflection is found to be about 5° for μ-mesons, produced at a height of 20000 m,

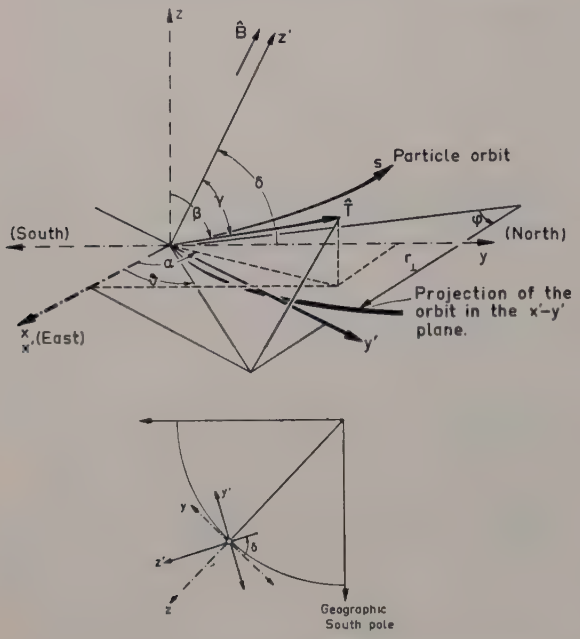

Fig. 22. Symbols used when calculating the magnetic deflection of secondary cosmic ray particles.

arriving at the earth from the zenith direction and having an energy of 1 GeV when they reach sea level. As about half of the μ-mesons are positively and half of them negatively charged [35] this deflection means a spread of the meson flow perpendicular to the direction of the magnetic field, and changes the angular intensity distribution discussed in 2.1.3.2.

The deflection of low energy particles in the earth's magnetic field has been studied by Johnson [33]. Calculations of the deflection of secondaries at seal level have been made by Bowen [34].

In the following, an approximative formulae for the magnetic deflection is deduced by taking the particle energy as constant during the motion through the atmosphere and equal to the mean value of the energies at the production level and the recording apparatus.

The orbit of a positively charged particle moving towards the earth is calculated by treating the problem of a negative particle of the same mass moving in the opposite direction. Fig. 22 shows the situation. The z-axis in the x, y, z system is directed in the zenith direction at a given place of observation. The magnetic field B is parallel to the z'-axis of a x', y', z' system. The x'- and x-axis coincide and the x', y', z' system is turned an angle $(90° - \delta)$ around the x-axis. δ is the dip angle of the magnetic field. The direction of the orbit at the telescope is represented by $\hat{T}$ and the angles α and β define this direction in the x, y, z system. ϑ and γ are the corresponding angles in the x', y', z' system, and s is the path length taken from origin. As the particle energy is assumed constant during the motion, the orbit is a spiral on a cylindrical surface. The projection of the orbit in the x', y' plane is a circle with the radius of curvature $r_\perp$:

$$r_\perp = r_0 \sin \gamma, \tag{57}$$

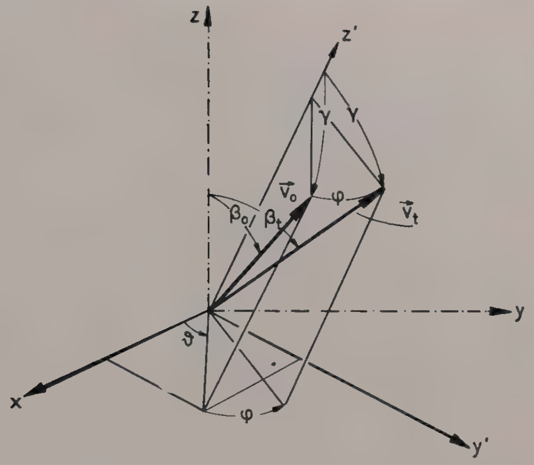

Fig. 23.

where $$r_0 = p/eB = (V/Bc)/\sqrt{1 + 2m_0c^2/eV}.$$

The following relations are found:

$$\cos\gamma = \sin\beta \sin\alpha \cos\delta + \sin\delta \cos\beta, \tag{58}$$

$$\sin\vartheta = \frac{\sin\delta \cos\gamma - \cos\beta}{\cos\delta \sin\gamma}. \tag{59}$$

The particle velocity is v. According to figs. 22 and 23 we have:

$$s = v\,t, \tag{60}$$

$$s\cos(\tfrac{1}{2}\pi - \gamma) = r_\perp \varphi, \tag{61}$$

$$z = \int_0^t v_t \cos\beta_t \, dt, \tag{62}$$

where v_t is the particle velocity at the time t and β_t is the angle between $\mathbf{v}_t$ and $\hat{\mathbf{z}}$.

We find from fig. 23 that:

$$\cos\beta_t = \sin\delta \cos\gamma - \cos\delta \sin\gamma \sin(\vartheta + \varphi), \tag{63}$$

which together with eq. 62 yields, as $v = v_t$:

$$z = \int_0^t v\,[\sin\delta \cos\gamma - \cos\delta \sin\gamma \sin(\vartheta + \varphi)]\, dt, \tag{64}$$

where φ is given by equations 60 and 61:

$$\varphi = (vt/r_\perp)\sin\gamma. \tag{65}$$

The solution of eq. 64 is:

$$z = r_0 \sin\gamma \cos\delta [\cos(\vartheta + s/r_0) - \cos\vartheta] + s \sin\delta \cos\gamma, \tag{66}$$

which gives the relation between the height of the production level z and the actual path length s.

For positively charged particles coming from the zenith direction ($\beta = 0$) at a place where $\delta = 0$ eq. 66 is reduced with equations 58 and 59:

$$z = r_0 \sin(s/r_0) \approx s[1 - \tfrac{1}{6}(s/r_0)^2]. \tag{67}$$

The direction of the orbit at a certain point is given by:

$$\alpha_t = \alpha + \Delta\alpha, \qquad \beta_t = \beta + \Delta\beta,$$

where $\Delta\alpha$ and $\Delta\beta$ are due to the magnetic deflection. We find from fig. 22 that:

$$\cos\beta_t = dz/ds, \tag{68}$$

$$\cos\alpha_t = (dx/ds)(1/\sin\beta_t). \tag{69}$$

Derivation of eq. 66 gives:

$$dz/ds = \cos\beta_t = \sin\delta \cos\gamma - \sin\gamma \cos\delta \sin(\vartheta + s/r_0). \tag{70}$$

The following expressions for α_t is found in an analogous way:

$$\cos\alpha_t = \frac{\sin\gamma \cos(\vartheta + s/r_0)}{\sin\beta_t}. \tag{71}$$

For positively charged particles coming from the zenith direction ($\beta = 0$) and with $\delta = 0$ eq. 70 is reduced to:

$$\cos\beta_t = \cos(s/r_0) \tag{72}$$

or

$$\beta_t = s/r_0,$$

which is obvious.

For a μ-meson starting at 20 km height and reaching the apparatus with an energy of $W_1 = 1$ GeV the angular deflection is found to be 4.6° using eq. 70, a mean energy of 1.9 GeV and a magnetic field of 0.3 gauss.

Bonnevier has taken the energy dependence of the covered path length into account and the more exact formulae are deduced by him and given in appendix. A comparison between values of the angular deflection of μ-mesons calculated using both the approximative and the more exact formula is shown in the following table; where the mesons have been assumed to have an energy of 1 GeV when they arrive at the telescope:

Hight of μ-meson production (m)	Angular deflection	
	Approx. formula	Exact formula
30 000	7.5°	6.6°
20 000	5.2°	4.6°
15 000	3.9°	3.7°
10 000	2.9°	3.1°

The approximate formula is good enough for our purpose when discussing the magnetic spread of the μ-meson flow at the equator. The deflection as a function

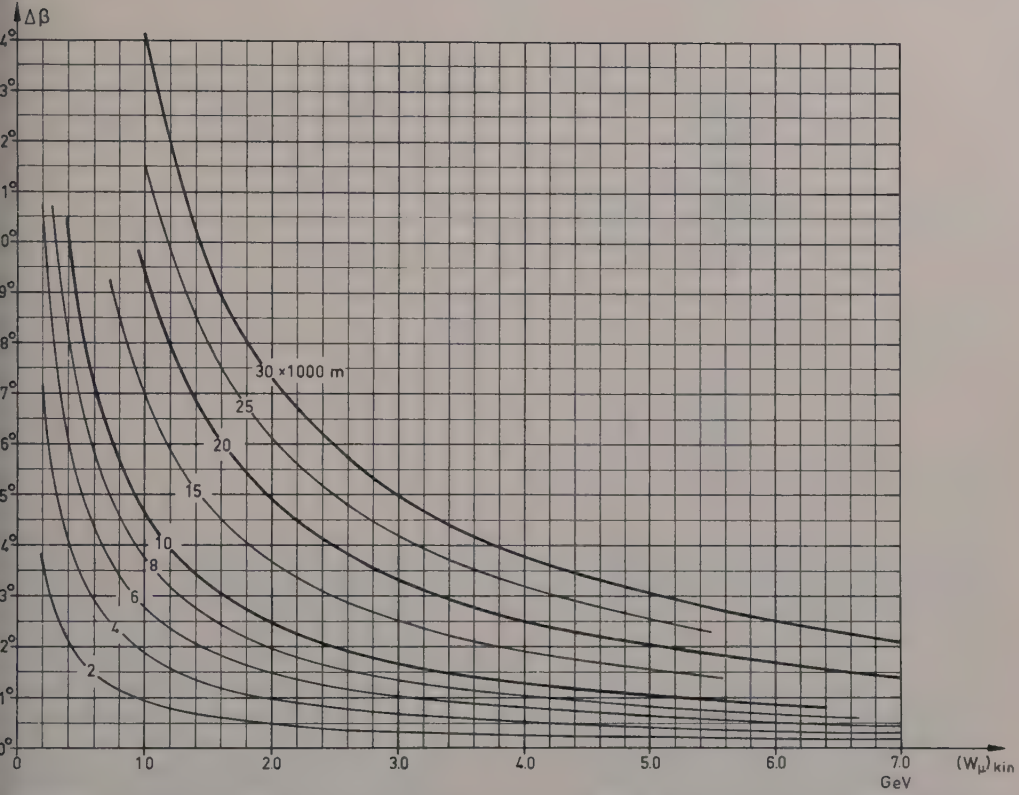

Fig. 24. The angular deflection of μ-mesons in a magnetic field of 0.3 gauss perpendicular to the motion. The mesons start at different heights and arrive at the telescope from the zenith direction. Their energy is constant during the motion, and equal to the mean value of the energies at the production level and the telescope.

of the μ-meson energy for mesons starting at different heights is plotted in fig. 24. The meson energy is assumed constant during the motion.

The effect of the magnetic deflection upon the image recorded by a zenith pointing, infinitely narrow angle telescope at the equator is estimated when the source is assumed to lie in the earth's equatorial plane. The angular intensity distributions of μ-mesons orginating from different production levels and recorded by the telescope as shown in fig. 19, are used together with the corresponding μ-meson energies (fig. 18). The angular deflection of mesons of different energies between the production level and the telescope is calculated for different production levels and is found to vary, for instance: 1°–4° at 10000 m, and the meson energies corresponding to the energy case $\gamma'_\pi = 10.00$. The lower value corresponds to μ-mesons which move in directions which deviate little from the primary direction ($\theta \approx 0$).

The angular deflection $\Delta\theta$ is thus a function of θ, the angle between the primary particle direction and the direction of the produced μ-mesons:

$$\Delta\theta = \vartheta(\theta).$$

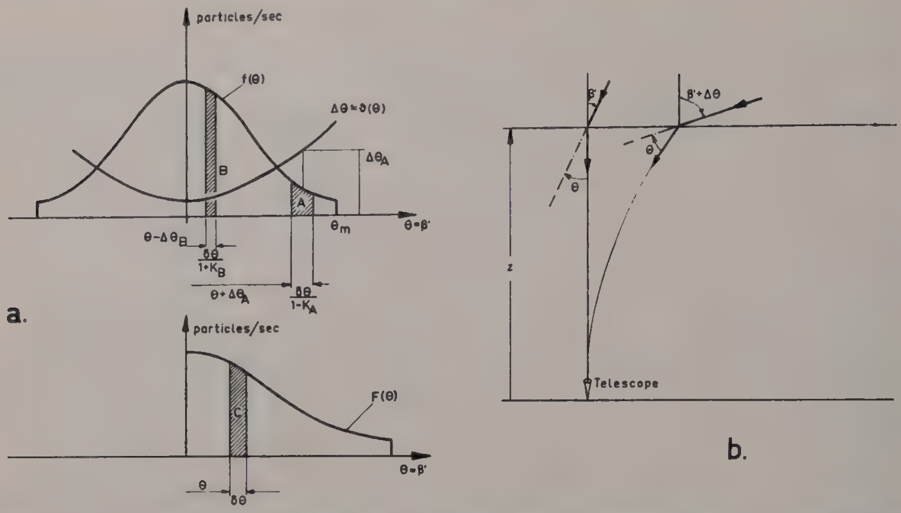

Fig. 25. (*a*) $f(\theta)$ is the intensity distribution recorded by the telescope when the earth rotates, assuming no magnetic field. $\Delta\theta = \vartheta(\theta)$ is the magnetic deflection of the mesons. $F(\theta)$ is the recorded intensity when the magnetic deflection has been taken into account.

(*b*) This shows the path of a μ-meson without (*left*) and with (*right*) the influence of the magnetic field.

The angular intensity distribution at sea level, corresponding to a certain level of production and modified by the deflection of the mesons, is found by the following consideration, see fig. 25.

$f(\theta)$ is the given distribution and $F(\theta)$ is the distribution modified by the magnetic deflection. We consider in fig. 25*a* the element $F(\theta)\,\delta\theta$ which is called C. This element represents the number of particles recorded by the telescope during the time interval when the earth rotates through the angle $\delta\theta$. Particles within the element C originate by deflection from the two elements A and B of the function $f(\theta)$. The elements A and B are at the angular distances $\Delta\theta_A$ and $\Delta\theta_B$ respectively from the element C.

First we must find the relationship between the shape and position of the element C and the shapes and positions of the two elements A and B. Using fig. 26 we deduce the relationship between an original element $f(\theta)\,\delta\theta$ and the two parts into which this element is divided by the magnetic deflection. Fig. 26*a* shows the original element; fig. 26*b* shows the variation of magnetic deflection with θ; and in fig. 26*c* are shown the two parts into which the original element has been split. It is seen from fig. 26 that the angular extensions along θ of the two resulting parts are, respectively,

$$\delta\theta\{1 - d(\Delta\theta)/d\theta\} \quad \text{and} \quad \delta\theta\{1 + d(\Delta\theta)/d\theta\}.$$

From the above it is clear that the angular intervals of the elements A and B in fig. 25 are $\delta\theta/(1 - k_A)$ and $\delta\theta/(1 + k_B)$ respectively, where $k = d(\Delta\theta)/d\theta$.

Subscripts refer to the derivatives at A and B. As half the number of the particles are deflected in both directions from both A and B, we get:

$$F(\theta)\,\delta\theta = \tfrac{1}{2}\left[f(\theta - \Delta\theta_B)\,\frac{\delta\theta}{1 + k_B} + f(\theta + \Delta\theta_A)\,\frac{\delta\theta}{1 - k_A}\right] \tag{73}$$

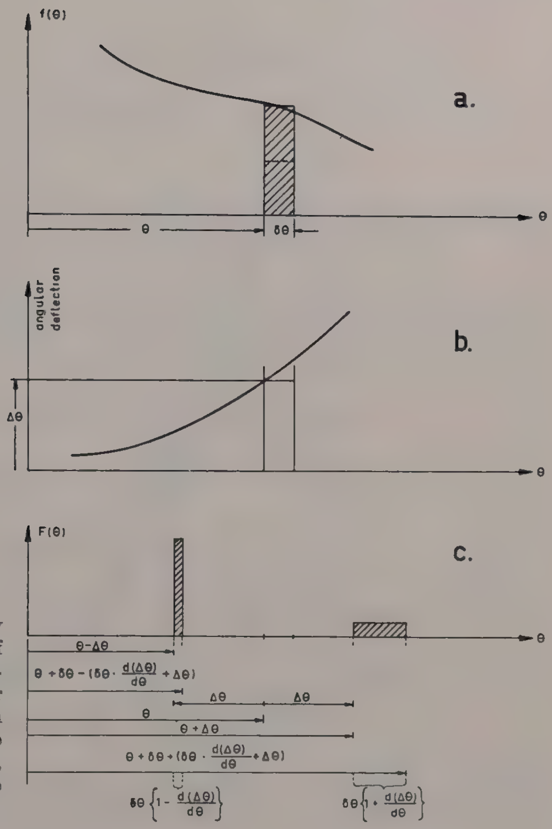

Fig. 26. (*a*) $f(\theta)$ is the measured intensity at sea level if the magnetic deflection of the μ-mesons is neglected. (*b*) The variation of the angular deflection with θ for mesons coming from a given production level. (*c*) The two elements shown are those into which the original element, $f(\theta)\,\delta\theta$, of figure 26*a* is divided by the magnetic field.

(In the actual calculations we always have $k < 1$.)

or:

$$F(\theta) = \tfrac{1}{2}\left[\frac{f(\theta - \Delta\theta_B)}{1 + k_B} + \frac{f(\theta + \Delta\theta_A)}{1 - k_A}\right]. \tag{74}$$

If $f(\theta) = 0$ for $\theta > \theta_m$ where θ_m is a cut-off value for the given function $f(\theta)$ we get:

$$F(\theta) = \tfrac{1}{2}\,\frac{f(\theta - \Delta\theta_B)}{1 + k_B} \quad \text{for } \theta_m < \theta < \theta_m + \Delta\theta_A \tag{75}$$

and

$$F(\theta) = 0 \quad \text{for } \theta > \theta_m + \Delta\theta_A.$$

Furthermore we have from fig. 25*a* the conditions:

$$\vartheta(\theta + \Delta\theta_A) = \Delta\theta_A, \tag{76}$$

$$\vartheta(\theta - \Delta\theta_B) = \Delta\theta_B. \tag{77}$$

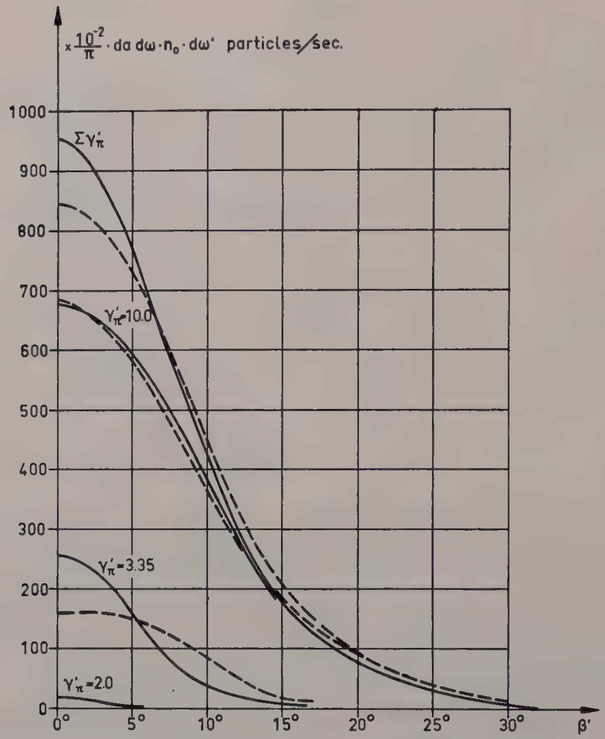

Fig. 27. The change in the angular intensity distribution due to geomagnetic deflection of the μ-meson flow. Full drawn curves show undeflected (compare fig. 20) and dashed curves deflected distribution.

The influence of the deflection has then been estimated by introducing the following two approximations:

$$\vartheta(\theta) = \pm k\theta + l, \tag{78}$$

$$f(\theta) = a \exp(-\theta^2/b^2). \tag{79}$$

This gives:

$$F(\theta) = \frac{a}{2}\left\{\frac{\exp\left[-\frac{1}{b^2}\left(\theta - \frac{\Delta\theta}{1+k}\right)^2\right]}{1+k} + \frac{\exp\left[-\frac{1}{b^2}\left(\theta + \frac{\Delta\theta}{1-k}\right)^2\right]}{1-k}\right\} \tag{80}$$

where $\Delta\theta$ is the deflection at θ.

$\Delta I(\theta) = f(\theta) - F(\theta)$ has been calculated for each production level and the contributions from all levels added with the proper weight for the energy cases $\gamma'_\pi = 3.35$ and 10.0 as described in section 2.1.3.2.

The found difference has been added to the intensity distributions obtained in section 2.1.3.2 and the resulting distributions are shown in fig. 27, where also the original distributions have been plotted.

The influence of the deflection on the resulting distribution, $\Sigma_{\gamma'_\pi}$, is not very important and has been neglected in the calculations.

2.2. The polar diagram of telescopes of finite dimensions when the geomagnetic influence on the primary particles is neglected

It is now possible by using the integral eq. 49 of section 2.1.3.2 to calculate the polar diagram of a telescope of finite aperture. With the abbreviations in section 2.1.3.2 the integral is written:

$$d^4 n_\mu = da\, d\omega\, n_0\, d\omega'\, K(\theta, W_p, z)\, dz, \tag{81}$$

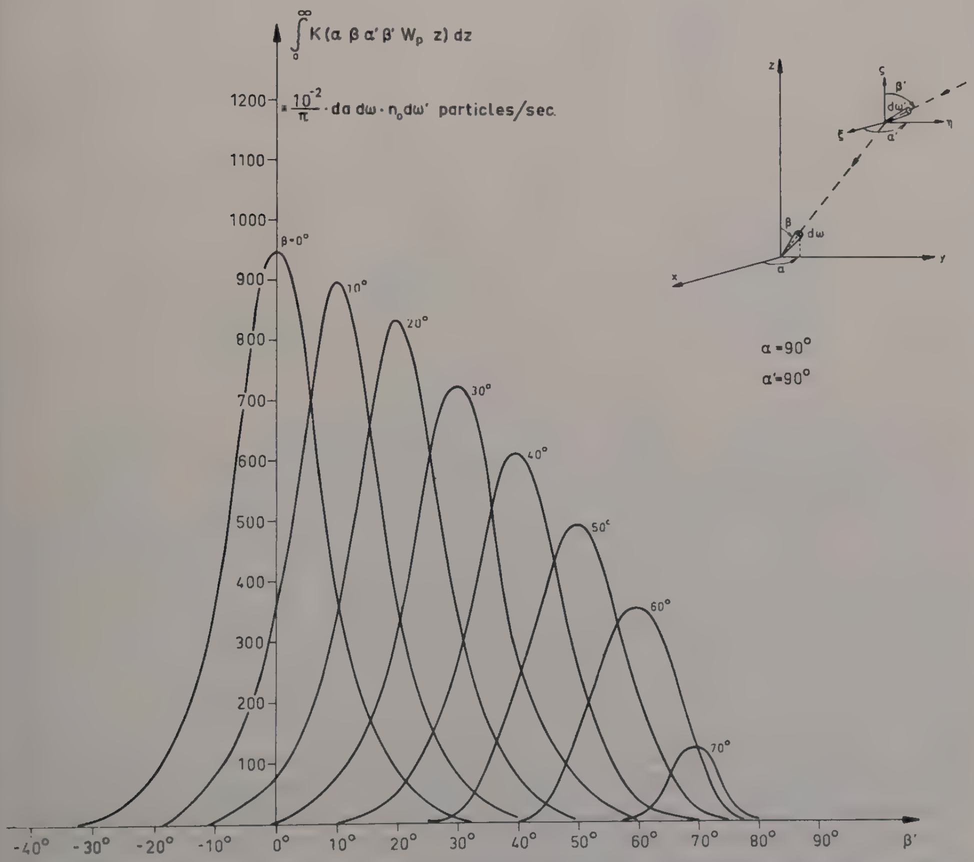

Fig. 28*a*. Polar diagrams of a telescope with infinitely small solid angle, when the geomagnetic influence is neglected i.e. the intensity measured by a telescope *da dω* tilted at different angles *β* to the vertical as a function of *β'*, the zenith angle of the primary beam. The azimuth angle of the telescope, α = 90°.

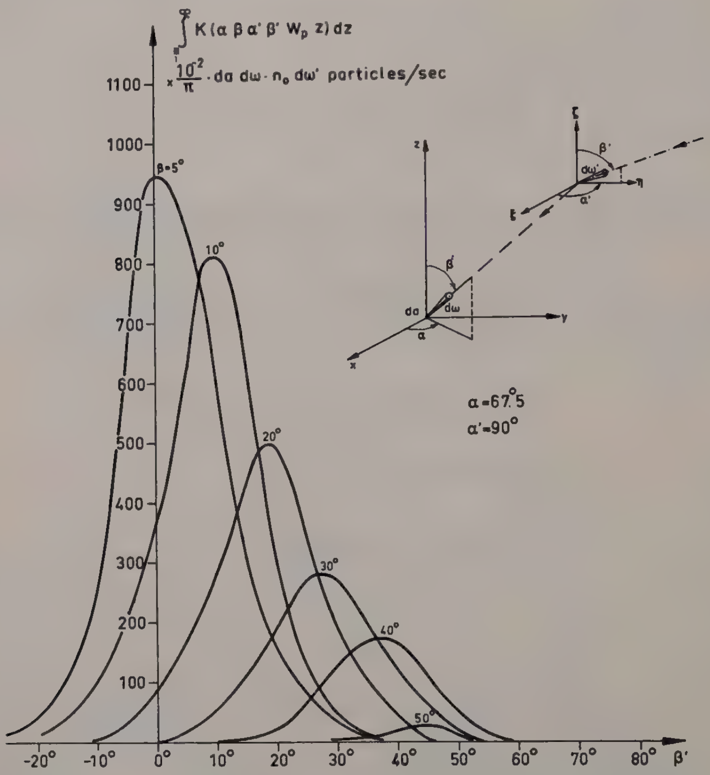

Fig. 28*b*. As in fig 28*a*, with $\alpha = 67.5°$.

where θ is a function of α, β, α' and β' according to eq. 50 and $d\omega = \sin\beta \, d\alpha \, d\beta$.

For a zenith pointing, cylindrical telescope at sea level the counting rate due to the primary beam is:

$$dn_\mu = n_0 \, d\omega' \int_{\alpha=0}^{2\pi} \int_{\beta=0}^{u_{\max}} \sin\beta \, d\alpha \, d\beta \int_a da \cos\beta \int_{z=0}^{\infty} K(\theta, W_p, z) \, dz. \tag{82}$$

The effective measuring surface is (compare 1.4.1.):

$$\int_a \cos\beta \, da = a \cos\beta \, G(\beta).$$

The rest of the integral has been solved with numerical calculations. The integral was first solved for different measuring directions in zenith as well as in azimuth for a telescope with infinitely small solid angle and for different directions of the primary beam. The result thus obtained is the polar diagram of a telescope with infinitely small solid angle pointing in different directions and situated at the equator, the source being in the equatorial plane. This is shown in figures 28*a* and 28*b* for two azimuth directions and for a number of zenith directions. The polar diagram of a finite telescope has been obtained with the help of these and similar diagrams.

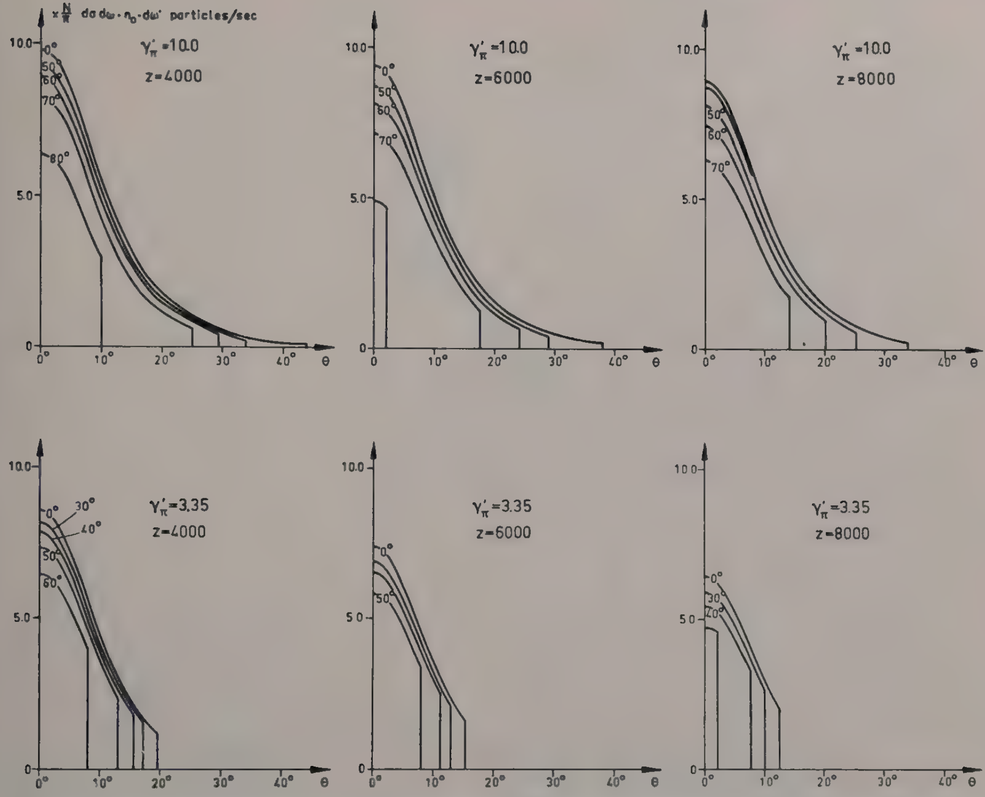

Fig. 29. The contributions to the counting rate of different production levels z and two different π-meson energies in the C-system.

The integration giving the polar diagrams in fig. 28 has been done as follows: The atmosphere was divided into a number of horizontal layers of finite thickness $\Delta z = 2000$ m. For each layer a set of curves was calculated which give the counting rate of the telescope pointing in different directions when recording μ-mesons which have started towards the telescope with different energies from the center of the layer. For a certain π-meson energy in the C-system these energies are given by the angle θ between the primary particle beam and the direction of the meson flow produced as discussed in section 2.1.2. As an example a few diagrams corresponding to π-meson energies $\gamma_\pi' = 10.0$ and 3.35 in C-system are shown in fig. 29. Both the decay and the absorption have been taken into account (the functions D and J of eq. 49). The production rate represented by the function R is however still put equal to one. Diagrams of this type have been computed for three π-meson energies in the C-system, namely $\gamma_\pi' = 10.0$, 3.35 and 2.00. As these energies were chosen so as to represent the same number of mesons within the corresponding energy intervals (compare 2.1.2) the curves in fig. 29 belonging to the same atmospheric layer have been added with the same weight. The combined diagram represents, approximately, the total counting rate of the infinitely narrow angle telescope due to meson production within the given layer.

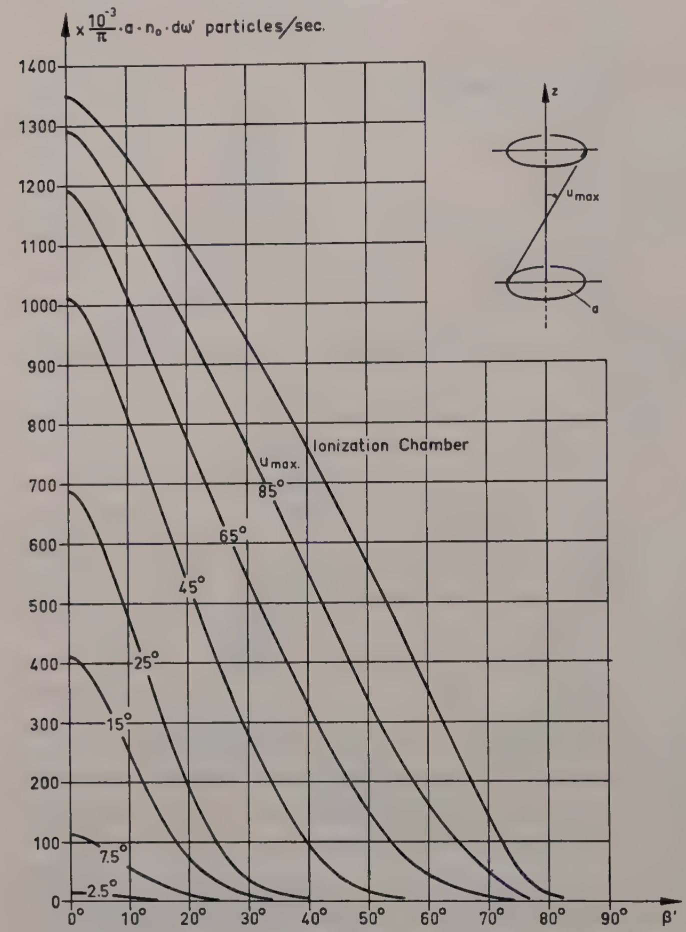

Fig. 30. The counting rate of zenith pointing telescopes with different apertures as a function of the zenith angle of incidence β' of the primary beam. As β' equals Ψ, the longitudinal position of the source, these are the polar diagrams for $\Phi = 0$ when the geomagnetic influence is neglected. These functions are designated $Q(\beta', W_p, u_{\max})$.

The next step was to summate the contributions from all layers in the atmosphere with regard to the variation of production rate. For a given direction of the primary beam (α', β') and measuring direction of the telescope (α, β) the angle θ was obtained from eq. 50. The contribution from each layer was then calculated by taking the counting rate from the combined diagrams of fig. 29, multiplied by the value of the function R for the corresponding layer. This was repeated for all layers up to a height above which there is no contribution to the counting rate.

The procedure was repeated for a number of measuring directions α and β and different angles of incidence β' of the primary beam. As the telescope was assumed, for simplicity, to be situated at the equator, α' of the primary beam is always 90° and β' equals the longitude angle Ψ of the source. We thus finally arrive at the diagrams of the type already shown in figures 28*a* and 28*b*, which have been computed for $\beta = 0°, 10° \dots 80°$ and $\alpha = \pm 90°, \pm 67.5°, \pm 45.0°, \pm 22.5°, 0°$. These curves are solutions to the integral of eq. 82:

$$\int_{z=0}^{\infty} K(\theta, W_p, z)\, dz.$$

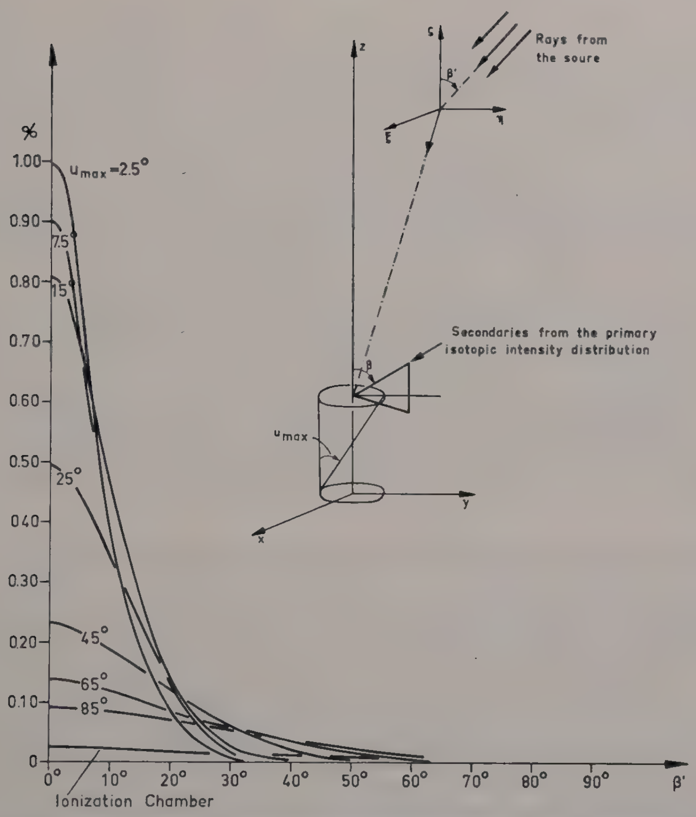

Fig. 31. The percentage increase of the counting rate when measuring a very small source element with telescopes of different apertures. The $\cos^2 \beta$ law is assumed to hold at sea level for the intensity distribution of the "background".

The case of a finite telescope can now be tackled using these diagrams and requires an integration over $d a\, d\omega$ in eq. 81. Our cylindrical telescope was assumed to point in the zenith direction. Its total solid angle was divided into a number of sections both in zenith and azimuth, each section being centred at those values of α and β for which the counting rate of an infinitely narrow angle telescope had been computed. The total counting rate for a given direction β' of the primary beam was then found by summing up the contributions from all the parts of the solid angle. The values of the counting rate for each part were taken from the above mentioned diagrams and multiplied by the value of the function $\cos u\, G(u)$ for the mean direction β of the section in order to allow for the effective measuring telescope surface in the same way as described in section 1.4. The result is plotted in fig. 30.

When applying these results to the measurements of daily variations it must be pointed out that what we actually observe, when measuring with cosmic ray telescopes, is the ratio between source and background intensities and not the source intensity itself [36]. If we were to measure an amplitude, of say 1 %, in the daily variation with an infinitely narrow angle telescope, assuming the source which causes this daily variation to subtend an infinitely small solid angle, then a broad angle telescope measures a smaller amplitude, because it records a higher "background".

According to fig. 28*a* a telescope ($da\,d\omega$) pointing in the zenith direction records a maximum counting rate of

$$(9.45/\pi)da\,d\omega\,n_0\,\Delta\omega' \quad \text{particles/sec}$$

due to the source which subtends the small solid angle $\Delta\omega'$. If we assume the ratio between the counting rates of source and background intensities to be 1 % we get:

$$n_0\,\Delta\omega'/I_0 = \pi/945. \tag{83}$$

The counting rate of cylindrical telescopes due to the background is calculated in appendix IV assuming the $\cos^2\beta$ law to hold. The result is plotted in fig. AIV.1.

With the relation in eq. 83 and with fig. AIV.1. the relative counting rate of source and back ground intensities recorded by telescopes of different apertures has been calculated from fig. 30. The result is shown in fig. 31, where the big difference between a narrow angle telescope and an ionization chamber should be noticed.(¹)

2.3. The zenith angle dependence of the radiation at sea level

The variation of the counting rate of a telescope with the zenith angle β is found experimentally to be approximately a $\cos^2\beta$ curve at sea level [38 and 39]. This fact offers a valuable check of the calculations as regards the atmospheric part and has been carried out for a narrow angle telescope assuming isotropic distribution of point sources over the hemisphere using the described calculations. The result is shown in fig. 32 where the $\cos\beta$, $\cos^2\beta$ and $\cos^3\beta$ curves have been drawn for comparison. The calculated curve agrees fairly well with the $\cos^2\beta$ curve. The rather good agreement indicates that the assumptions regarding the meson production and the primary energy of 20 GeV give an essentially representative picture of the phenomena in the atmosphere.

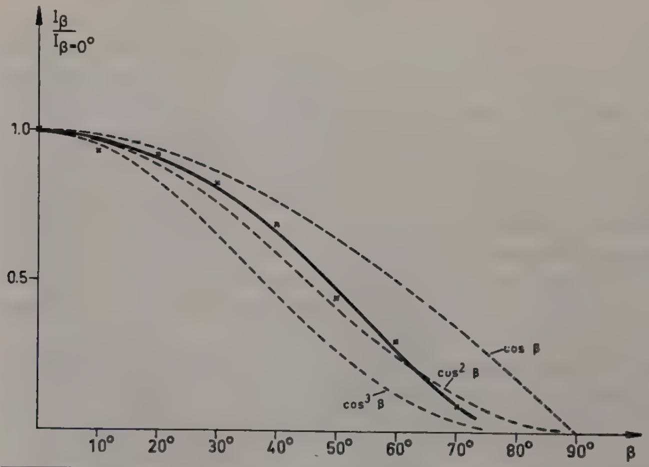

Fig. 32. The zenith angle dependence of the cosmic ray intensity at sea level. Crosses are calculated values.

(¹) Amplitudes of the order of 1 % in the daily intensity variation using narrow angle telescope have been reported by Sarabhai [37]. Such results could be explained by these calculations.

A few remarks should be made in connection with the zenith angle dependence of the radiation. The first one applies to ionization chambers. It is well known that the maximum contribution to the counting rate of an ionization chamber per unit of the zenith arc comes from directions between two concentric cones centered around the zenith direction and defined by the apex angles 2β and $2(\beta + d\beta)$ where $\beta = 35°$ if the $\cos^2\beta$ law holds for the radiation. It is obvious that this direction has no practical significance when discussing the directional properties of the chamber. Its most sensitive measuring direction is in the zenith direction and only in a hypothetical case when the whole particle flow is varying with time in the same way in all directions can we talk about $\beta = 35°$ as the most sensitive direction.

Another remarkable point is the following. A narrow angle telescope is tilted at an angle β to the zenith direction. Its counting rate due to the background radiation is:

$$\nu = N_0 \cos^2\beta \quad \text{particles/sec},$$

where N_0 is the counting rate when pointing in the zenith direction. A change in β means a change in the measured intensity according to:

$$\Delta\nu/\nu = -2 \operatorname{tg} \beta \, \Delta\beta.$$

A percentage change in the counting rate of say 0.1 % at $\beta = 45°$ corresponds to a change in $\Delta\beta$ of 0.03°. Daily changes in the measuring direction of this order of magnitude could introduce considerable errors in the image of a cosmic ray source. It is consequently important that a tilted telescope is mounted in a stable way.

3. THE COMPLETE POLAR DIAGRAM OF A COSMIC RAY TELESCOPE

At this stage we are able to discuss the complete polar diagram of a cosmic ray telescope taking into account both the geomagnetic deflection and the influence of the atmosphere.

The angular position of a source element on the sphere of asymptotic directions is given by Ψ and Φ; the position determines the direction of incidence (α', β') of the primary beam at the top of atmosphere (see fig. 10). The intensity of the beam is

$$dn_0 = I(p)\,dp \quad \text{particles/cm}^2\cdot\text{sec}\cdot\text{sterad},$$

and the beam subtends the solid angle (cf. eq. 18b) $\Delta\omega' = M \cdot \Delta\Omega$ where $\Delta\Omega$ is the solid angle subtended by the source element. $I(p)$ represents, as before, the primary differential momentum spectrum of the source and M the magnification of the geomagnetic field.

Secondaries are recorded by the given telescope provided the source element is within the projected *extended* solid angle of the telescope on the sphere of asymptotic directions for a certain momentum p. This solid angle extends beyond the projected total solid angle defined in section 1.4 due to the influence of atmosphere. The extension is found from fig. 30 when considering primary particles of momentum 20 GeV/c.

The beam intensity was introduced in section 2.1.1. and the counting rate of the telescope at sea level is found from eq. 81 in section 2.2 when the atmospheric influence is taken into account. The contribution to the counting rate from a surface element da of the telescope and solid angle $d\omega$ due to μ-mesons produced by primaries within the momentum interval dp is consequently:

$$d^3 n_\mu = I(p)\, dp\, \Delta\omega'\, da \cos u\, d\omega \int_0^\infty K(\theta, W_p, z)\, dz. \tag{84}$$

The direction of $d\omega$ is given by α and β. As the cylindrical telescope points in the zenith direction we have $u = \beta$. θ is a function of α, β, α' and β' given by eq. 50.

Integration over the whole telescope surface yields:

$$d^2 n_\mu = I(p)\, dp\, \Delta\omega'\, a \cos\beta\, G(\beta)\, d\omega \int_0^\infty K(\theta, W_p, z)\, dz, \tag{85}$$

which is the counting rate of the telescope for μ-mesons arriving within the solid angle $d\omega$ (compare eq. 20).

Integration over the total solid angle of the telescope gives finally:

$$dn_\mu = I(p)\, dp\, M\, \Delta\Omega\, a \left[\int_{\alpha=0}^{2\pi} \int_{\beta=0}^{u_{\max}} \cos\beta\, G(\beta) \sin\beta\, d\alpha\, d\beta \int_0^\infty K(\theta, W_p, z)\, dz \right] \cdot \tag{86}$$

The function within the brackets, $Q(\beta', W_p, u_{\max})$, was solved for telescopes with different apertures $u_{\max}$ in section 2.2 and plotted in fig. 30. The counting rate due to primaries in a momentum interval dp at p is obtained from eq. 86. The value of β' is given by the angular position Ψ and Φ of the source element on the sphere of asymptotic directions. (The value of α' is of no importance as the telescope is assumed to point in the zenith direction.) M is taken from diagrams of the type shown in fig. 8 b. Contributions from all momentum intervals for which $Q(\beta', W_p, u_{\max}) \neq 0$ give the total counting rate and thus the value of P at Ψ, Φ, giving the complete polar diagram when both the geomagnetic deflection of the primaries and the influence of the atmosphere have been taken into account.

Let us however discuss eq. 86 once more with particular reference to the function $K(\theta, W_p, z)$. As $M\, \Delta\Omega$ is independent of both α and β, eq. 86 is also written:

$$dn_\mu = \int_{\alpha=0}^{2\pi} \int_{\beta=0}^{u_{\max}} a \cos\beta\, G(\beta) \sin\beta\, d\alpha\, d\beta\, I(p)\, dp\, M\, \Delta\Omega \int_0^\infty K(\alpha, \beta, \alpha', \beta', W_p, z)\, dz, \tag{87}$$

where

$$I(p)\, dp\, M\, \Delta\Omega \int_0^\infty K(\alpha, \beta, \alpha', \beta', W_p, z)\, dz \tag{88}$$

represents the number of μ-mesons arriving at the telescope from the direction α,β produced by primary particles which come from the direction α',β'. The integral was solved in section 2.2 for $W_p = 20$ GeV and plotted in fig. 28. It relates the number of μ-mesons measured in direction α,β at sea level to the number of primaries at the top of the atmosphere coming from the direction α',β'.

A function which relates the measured number of one sort of secondary particle, for example μ-mesons to the number of primaries within different momentum intervals, is called "the over-all multiplicity" by Neher [40] or "yield function" by Simpson *et al.* [41].

Assuming the earth's field to be a dipole field, and by using this field as a magnetic analyzer for the arriving primary particles, it has been possible to deduce the yield

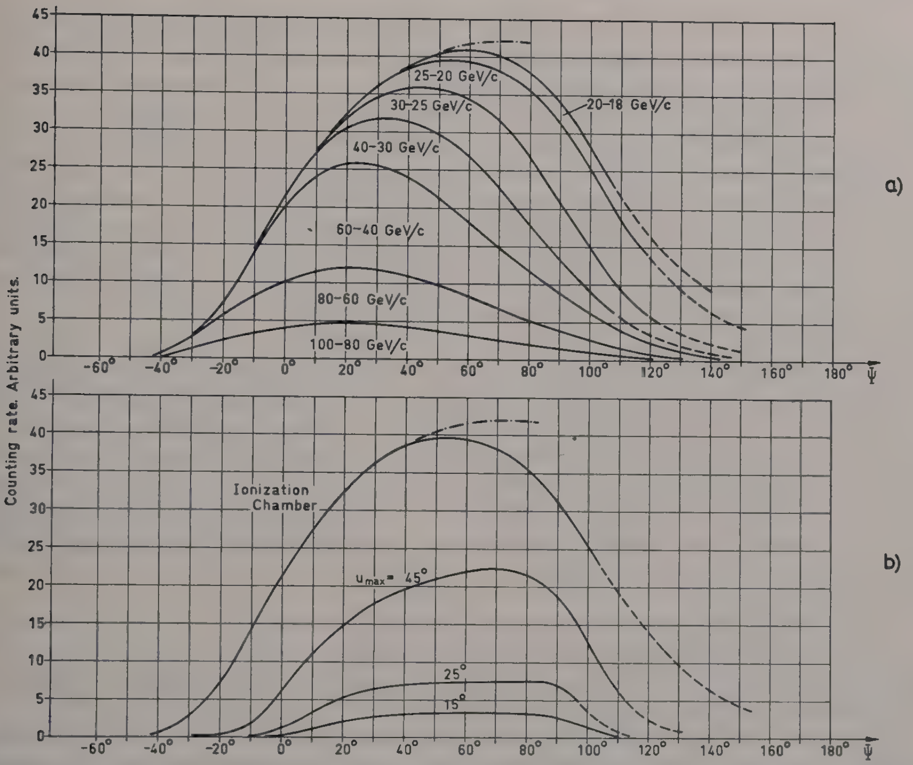

Fig. 33. (*a*) The contributions of different primary momentum intervals to the polar diagram along $\Phi = 0$ of an ionization chamber at sea level in Huancayo. (*b*) The polar diagrams along $\Phi = 0$ for telescopes with different apertures at sea level in Huancayo.

function from measurements of the latitude effect. This has been done by Neher [40] for the ionizing component and by Simpson *et al.* [41] for the nucleonic component; the yield functions obtained are those of the *isotropic* radiation. The yield function $Y(p,\beta)$ for the ionizing component derived by these authors is related to the one given in eq. 88 by:

$$Y(p,\beta) = \frac{1}{2\pi} \int_{\alpha'=0}^{2\pi} \int_{\beta'=0}^{\pi/2} \sin\beta'\, d\alpha'\, d\beta' \int_{0}^{\infty} K(\alpha,\beta,\alpha',\beta',W_p,z)\, dz. \tag{89}$$

$Y(p,\beta)$ is a mean function taken over all primary directions α' and β' in the hemisphere which are not forbidden for particles with momentum p.

The yield function derived for an ionization chamber is still more complex:

$$Y_i(p) = \frac{1}{2\pi} \int_{\alpha=0}^{2\pi} \int_{\beta=0}^{\pi/2} Y(p,\beta) \sin\beta\, d\alpha\, d\beta \tag{90}$$

The yield function times the primary spectrum is called the effective primary spectrum. The effective primary spectrum of an ionization chamber defined in this way is known up to 13 GeV/c. Fonger [42] has deduced a spectrum above this point of the form $(1 + W_p)^{-1.2}$. The correct way of calculating the polar diagram is, however, to use eq. 86 taking into account the variation of W_p in the function $K(\theta, W_p, z)$.

This energy dependence means roughly that the energy available for meson production increases with the primary energy and also that the meson energies in the forward direction in the laboratory system are increased. Thus the mean energy of the μ-meson flow is an increasing function of the primary energy. Due to absorption and decay, fewer μ-mesons reach sea level per given number of primaries in the lower primary energy range. This corresponds to a decrease of the yield function with decreasing energy.

The variation of W_p has been taken into account approximately by using the Fonger-spectrum $(1 + W_p)^{-1.2}$ when calculating the complete polar diagram at sea level shown in fig. 33. The error introduced by this approximation is probably of minor importance at present compared to the errors introduced by our lack of knowledge about the geomagnetic deflection in the low momentum range. It is also assumed that the function Q is independent of W_p and the solutions for $W_p = 20$ GeV have been used. This assumption introduces an error which is of little importance for the shape of the polar diagrams when considering apertures larger than 15° and energies above 20 GeV.

It is, however, possible to solve the equations presented in this paper for other values of the primary energy than 20 GeV and thus take the energy dependence into consideration in a more correct way than by using the effective primary spectrum integrated over all primary directions.

The polar diagrams of fig. 33 are of fundamental importance when calculating the image of a cosmic ray source lying in the equatorial plane. On the other hand when the image is given, the polar diagrams are used to correct for the influence of the geomagnetic field and the atmospheric spread, thus finding the real angular position in space and the shape of the source. This is further discussed in section 3.1 and chapter 4.

3.1. The image of a source element obtained by using the polar diagram

Consider a source element infinitely far away from the earth in the equatorial plane. Its angular position is given by Ψ' which is an easterly longitudinal angle reckoned from the sun-earth line, see fig. 34*b*. When the earth rotates the image of the source is given by the polar diagram $P(\Psi, \Phi = 0)$ as in fig. 34*a*. Since Ψ is taken as increasing in an easterly direction, we find that the shape of the image is the reverse of that of the polar diagram.

4. THE RESOLVING POWER OF COSMIC RAY TELESCOPES

As in ordinary optics, the resolving power of a cosmic ray telescope could be defined as the smallest distinguishable angular distance $\delta(\omega t)$ between two cosmic ray source elements, as in fig. 35. The criterion of observability could be the statistical significance of $\delta N/N_0$ in the figure. This should mean that the resolving power depends on

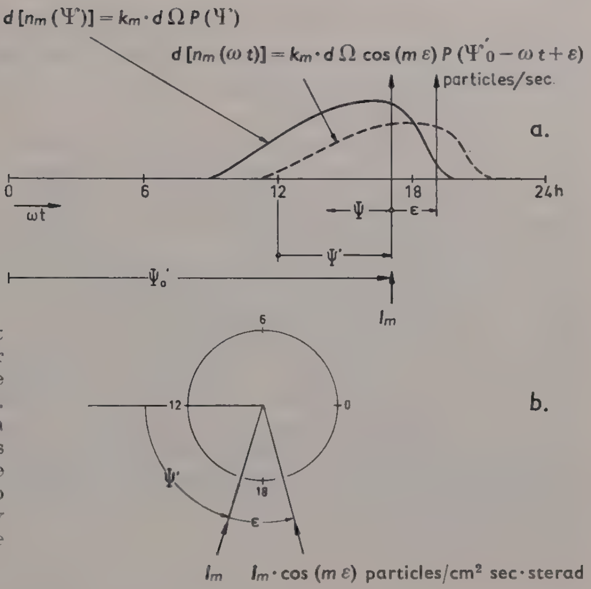
d [n_m (Ψ')] = k_m · d Ω P (Ψ')
d [n_m (ω t)] = k_m · d Ω cos (m ε) P (Ψ'_0 − ω t + ε)
particles/sec.
a.
0
6
12
18
24h
ωt
Ψ
ε
Ψ'
Ψ'_0
I_m
6
12
0
18
b.
Ψ'
ε
I_m
I_m · cos (m ε) particles/cm² sec · sterad

Fig. 34. The image of a source element recorded by a telescope using its polar diagram. The fulldrawn curve is the image of a source in the direction Ψ'. The dashed curve corresponds to a source in the direction $\Psi' + \varepsilon$. $d\,\Omega$ is the solid angle subtended by the source element. k_m is proportional to the amplitude of the mth intensity distribution and to the surface of the telescope.

the geomagnetic position and aperture of the telescope which together determine the polar diagram and consequently the image of a source element. It also depends on the size of the telescope measuring surface as this, together with the aperture, determines the magnitude of the counting rate. For a given surface, a wide aperture gives a high counting rate, and the statistical determination of $\delta N/N_0$ is more accurate than with a narrow aperture and the same surface. But a wide aperture means also a polar diagram with large extension along the Ψ'-axis as has been shown in the preceding chapters. The image obtained is consequently broad which reduces $\delta N/N_0$. Thus a compromise is required; the optimum aperture being found empirically.

A more practicle definition of resolving power is the capability of the telescope to

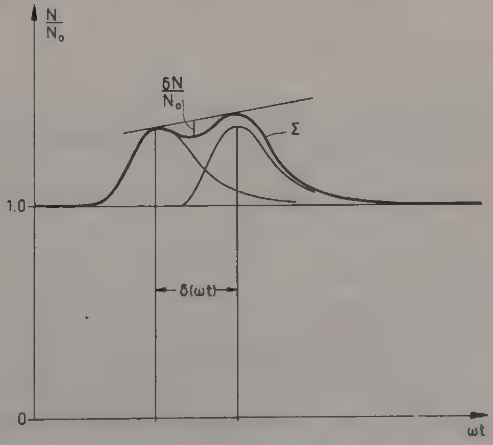

Fig. 35. The resulting image, Σ, of two source elements at an angular distance $\delta(\omega t)$ apart. ω is the angular velocity of the earth. N_0 is the counting rate due to the isotropic background.

reproduce higher harmonics in the extra-terrestrial intensity distribution. This definition is particularly convenient because the measured images are usually analyzed in terms of first and second harmonics which describe the angular extension of the source around the earth's axis.

Let us assume that the particle intensity around the earth varies sinusoidally with the period $m\,2\pi$ along the equator with maximum intensity I_m in a direction given by Ψ' which is an easterly longitudinal angle reckoned from the sun-earth line as in fig. 34. The longitudinal variation of intensity is represented by a distribution of source elements along the equator, all with the same momentum spectrum but with a source strength which varies sinusoidally with maximum intensity in the direction Ψ'. A source element subtending the solid angle $d\Omega$ produces an image as described in section 3.1. The images produced by different source elements are displaced relative to each other and all subtend the same angular interval along the time axis ωt but their magnitude depend on the corresponding source strength. The resulting image is obtained by integrating the contributions from all directions ε.

This is done by developing the function $P(\Psi,\Phi=0)$ in a Fourier series. Generally the image due to the source element subtending the solid angle $d\Omega$ at the angle $(\Psi'+\varepsilon)$ is:

$$k_m\,d\Omega\cos(m\varepsilon)\,P(\Psi'_0-\omega t+\varepsilon) = k_m\,d\Omega\cos(m\varepsilon)\sum_{\nu=0}^{\infty}P_\nu\cos[\nu(\Psi'_0-\omega t+\varepsilon)-\Psi_\nu], \qquad (91)$$

where $\Psi'_0=\Psi'+\pi$, see fig. 34. k_m is proportional to I_m and to the surface of the telescope.

m means the mth harmonic of the intensity distribution along the equator and P_ν denotes the different Fourier-coefficients of $P(\Psi,\Phi=0)$.

Keeping ωt constant we integrate the contributions from all directions ε with $d\Omega=d\varepsilon\,d\Phi$ where $d\Phi$ is the angular extension of the source element along a meridian:

$$d[n_m(\omega t)]=k_m\,d\Phi\int_0^{2\pi}\cos(m\varepsilon)\sum_{\nu=0}^{\infty}P_\nu\cos[\nu(\Psi'_0-\omega t+\varepsilon)-\Psi_\nu]\,d\varepsilon. \qquad (92)$$

For the νth term we have:

$$d[n_{m\nu}(\omega t)]=k_m d\Phi\int_0^{2\pi}P_\nu\cos(m\,\varepsilon)\cos[\nu(\Psi'_0-\omega t-\Psi_\nu/\nu)+\nu\,\varepsilon]\,d\varepsilon. \qquad (93)$$

Integration yields:

$$d[n_{m\nu}(\omega t)]=k_m d\Phi\,P_\nu\left\{\cos\vartheta_\nu\Big/_{0}^{2\pi}\left[\frac{\sin(m-\nu)\,\varepsilon}{2(m-\nu)}+\frac{\sin(m+\nu)\,\varepsilon}{2(\nu+m)}\right]+\right.$$
$$\left.+\sin\vartheta_\nu\Big/_{0}^{2\pi}\left[-\frac{\cos(\nu+m)\,\varepsilon}{2(\nu+m)}-\frac{\cos(\nu-m)\,\varepsilon}{2(\nu-m)}\right]\right\} \qquad (94)$$

with
$$\vartheta_\nu=\nu\left(\Psi'_0-\omega t-\frac{1}{\nu}\Psi_\nu\right).$$

The integral is different from zero only when $\nu=m$:

$$d[n_\nu(\omega t)]=k_m d\Phi\,P_\nu\,\pi\cos\left[m\left(\Psi'_0-\omega t-\frac{1}{\nu}\Psi_\nu\right)\right]. \qquad (95)$$

Thus the image of a sinusoidal intensity distribution along the equator is a sine wave with the same period as the period of the given distribution and with maximum amplitude at

$$\omega t = \Psi_0' - \frac{1}{\nu} \Psi_\nu. \tag{96}$$

Furthermore it is found from eq. 95 that the amplitude of the νth harmonic of the image is proportional to the amplitude of the νth harmonic of the polar diagram $P(\Psi,\Phi)$ when developed in a Fourier series.

The resolving power is consequently determined by the Fourier coefficients of the polar diagram of the telescope.

The counting rate due to a constant intensity along the equator which corresponds to $m=0$ is:

$$d[n_0(\omega t)] = k_0 \, d\Phi \, P_0 \, 2\pi. \tag{97}$$

Let us take an example and discuss what an ionization chamber at Huancayo measures. The polar diagram of fig. 33*b* in chapter 3 has been analyzed and the amplitudes of the zero, first, second and third harmonics are respectively in the units of fig. 33: $P_0 = 12.5$, $P_1 = 17.9$, $P_2 = 7.9$, and $P_3 = 1.3$. The maxima occur at $\Psi_1 = 54°$, $\Psi_2 = 2\ (55° + n \times 180°)$, and $\Psi_3 = 3\ (38° + n \times 120°)$.

If the intensity distribution along the equator varies as

$$\sum_m \frac{I_m}{I_0} \cos(m\varepsilon),$$

where $\sum_m I_m \cos(m\varepsilon)$ represents the anisotropy and I_0 the isotropic background, the relative amplitudes of the measured first, second and third harmonics, found form eqs. 95 and 97, are:

$$\frac{k_1}{k_0} \cdot \frac{1}{2} \cdot \frac{P_1}{P_0}, \qquad \frac{k_2}{k_0} \cdot \frac{1}{2} \cdot \frac{P_2}{P_0}, \qquad \frac{k_3}{k_0} \cdot \frac{1}{2} \cdot \frac{P_3}{P_0}.$$

With the values of P_ν in the actual case we get:

$$\frac{k_1}{k_0} \cdot 0.72, \qquad \frac{k_2}{k_0} \cdot 0.32, \qquad \frac{k_3}{k_0} \cdot 0.05.$$

Thus the amplitudes of the extra terrestrial intensity distribution are reduced approximately by these factors when measured with an ionization chamber at Huancayo. The approximation depends on the incomplete polar diagram which was used. As pointed out in section 1.4.4 its shape is not determined in the lower momentum range. The complete polar diagram will reduce the above figures and also change the angles of maxima Ψ_1, Ψ_2 and Ψ_3, giving an increase in the case of Ψ_1.

In the discussion, we have only considered an intensity distribution along the equator but we may also have a sinusoidal intensity distribution along a meridian. When the period of the distribution is 2π both along the equator and along a meridian, the total distribution around the earth corresponds to a case when the earth moves relative to the isotropic distribution of particles. The shape of the image is in this case not strictly the same as with a distribution only along the equator and has to be integrated over all values of Φ using the corresponding polar diagrams $P(\Psi,\Phi)$. But, as the projected solid angles on the sphere are mainly symmetrical around the equator and the main contribution to the counting rate comes from this region, the shape of the image will not differ greatly from the one treated above and in any case its extension along ωt will be the same.

APPENDIX

A I. Calculation of the effective measuring surface of a cylindrical telescope

The telescope configuration is shown in fig. AI.1. The shaded surface is:

$$S = 2r^2\left[\varphi_{\max} - \frac{\sin 2\varphi_{\max}}{2}\right] \tag{A I.1}$$

with $\varphi_{\max}$ given by: $$\cos\varphi_{\max} = \frac{d}{2r}\operatorname{tg} u.$$

We introduce:

$$G(u) = \frac{S}{a} = \frac{2}{\pi}\left[\varphi_{\max} - \frac{\sin 2\varphi_{\max}}{2}\right]. \tag{A I.2}$$

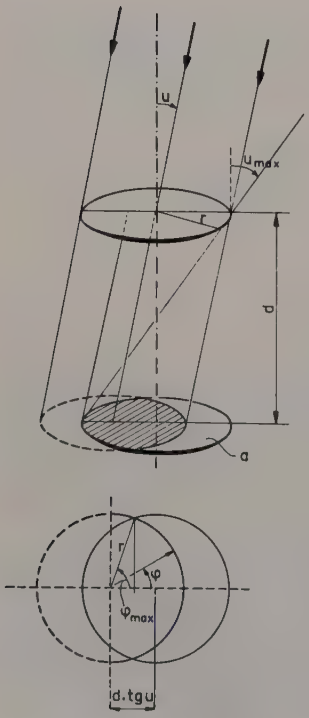

Fig. AI.1. The cylindrical telescope considered.

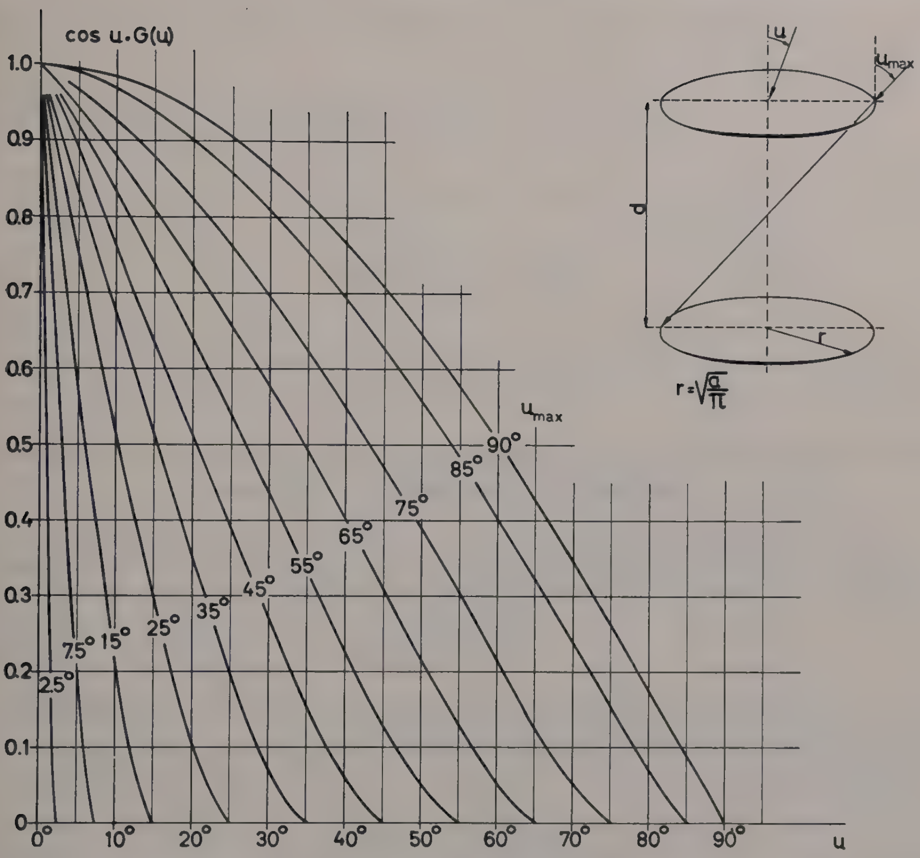

Fig. AI.2. The relative counting rates of telescopes with different apertures as a function of the angle of incidence.

The product cos $u\,G(u)$ is plotted in fig. AI.2 for different values of $u_{\max}$ and is the relative counting rate of a telescope which makes the angle u with the parallel beam of incident particles.

A II. The total production rate of secondaries in the atmosphere

Eq. 32 in section 2.1.1 is written:

$$\frac{dn}{dz} = -A \int_{\beta'=0}^{\frac{1}{2}\pi} \exp\left[-\left(B+\frac{C}{\cos\beta'}\right)\right] \operatorname{tg}\beta'\, d\beta' \qquad \text{(A II.1)}$$

with $$A = 2\pi\frac{n_0 m_0}{l L}, \qquad B = z/l, \qquad C = \frac{m_0 e^{-z/l}}{L}.$$

The integration is carried out for β' varying between 0 and $\frac{1}{2}\pi$ at a constant height z. Thus:

$$\frac{dn}{dz} = -A\,e^{-B}\int_0^{\pi/2}\exp\left(-\frac{C}{\cos\beta'}\right)\operatorname{tg}\beta'\,d\beta'. \tag{A II.2}$$

By the substitution $y = C/(\cos\beta')$ we get the integral:

$$\frac{dn}{dz} = A\,e^{-B}\int_C^{\infty}\frac{e^{-y}}{y}\,dy, \tag{A II.3}$$

which is tabulated in Jahnke–Emde [43]. dn/dz is plotted in fig. 13.

A III. Intensity and energy distributions in the laboratory system of π-mesons produced in nucleon-nucleon collisions

The intensity distribution $F(\theta, W_p)$ in the laboratory system (L-system) of secondaries, which are emitted at an angle θ to the direction of an arriving primary particle with energy W_p is given by Bradt, Kaplan and Peters [30]. Thus

$$dN = F(\theta, W_p)\,d\theta \tag{A III.1}$$

is the total number of secondaries emitted in directions between two concentric cones defined by the apex angles 2θ and $2(\theta + d\theta)$.

The number of secondaries emitted within a beam subtending the infinitely small solid angle $d\omega$ is:

$$dn = \frac{F(\theta, W_p)}{2\pi\sin\theta}\,d\omega = I(\theta, W_p)\,d\omega. \tag{A III.2}$$

The following symbols are used:

$$\alpha = \gamma_p'\operatorname{tg}\theta = \frac{\sin\theta'}{\cos\theta' + m} \tag{A III.3}$$

The prime denotes quantities in the centre of mass system (C-system). The subscript p refers to the proton.

$$\gamma = 1/\sqrt{1-\beta^2} \quad \text{with} \quad \beta = v/c, \tag{A III.4}$$

$$\gamma = 2(\gamma')^2 - 1, \tag{A III.5}$$

$$W'_{\text{tot}} = 2 m_p c^2 \gamma_p' = \text{total energy in } C\text{-system}, \tag{A III.6}$$

$$W_{\text{tot}} = m_p c^2 (1 + \gamma_p) = \text{total energy in } L\text{-system}, \tag{A III.7}$$

$$m = \frac{v_p'}{v_\pi'} = \frac{\text{velocity of proton in } C\text{-system}}{\text{velocity of } \pi\text{-meson in } C\text{-system}}. \tag{A III.8}$$

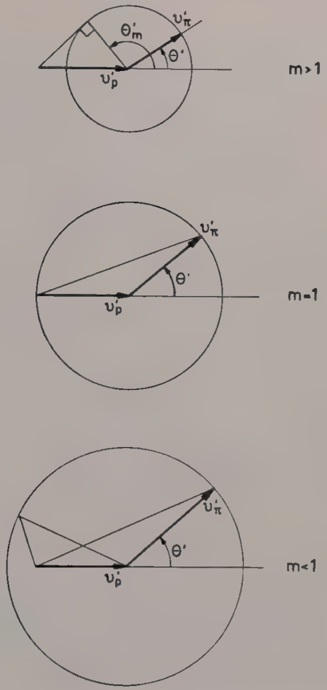

Fig. A III.1. The relation between the velocities of a proton and a π-meson in the centre of mass system of two colliding protons.

The average energy of mesons in L-system $\langle\gamma_\pi\rangle$ is related to the average energy in C-system $\langle\gamma'_\pi\rangle$ by:

$$\langle\gamma_\pi\rangle=\langle\gamma'_\pi\rangle\,\gamma'_p. \tag{A III.9}$$

We have to distinguish between three cases: $m>1$, $m=1$ or $m<1$ (see fig. A III.1).

$\boldsymbol{m>1}$

$$I(\theta, W_p)=\frac{N}{4\pi\sin\theta}\cdot\frac{\alpha}{(\alpha^2+1)^2}\cdot\frac{\gamma'_p}{\cos^2\theta}\cdot\frac{m^2+1-(m^2-1)\,\alpha^2\pm 2m\sqrt{1-(m^2-1)\,\alpha^2}}{\sqrt{1-(m^2-1)\,\alpha^2}} \tag{A III.10}$$

$$\gamma_\pi=\frac{(\gamma'_\pi/\gamma'_p)\,(\gamma'^2_p+\alpha^2)\pm\sqrt{\gamma'^2_\pi-1}\,\sqrt{\gamma'^2_p-1}\,\sqrt{1-(m^2-1)\,\alpha^2}}{\alpha^2+1}. \tag{A III.11}$$

The plus sign applies when $\theta'<\theta'_m$.
The minus sign applies when $\tfrac{1}{2}\pi>\theta'>\theta'_m$.

$\boldsymbol{m=1}$

$$I(\theta, W_p)=\frac{N}{\pi\sin\theta}\cdot\frac{\alpha}{(\alpha^2+1)^2}\cdot\frac{\gamma'_p}{\cos^2\theta}, \tag{A III.12}$$

$$\gamma_\pi=\frac{(\gamma'_\pi/\gamma'_p)\,(\gamma'^2_p+\alpha^2)+\sqrt{\gamma'^2_\pi-1}\,\sqrt{\gamma'^2_p-1}}{\alpha^2+1}. \tag{A III.13}$$

$m < 1$,

$\theta < \frac{1}{2}\pi$

$$I(\theta, W_p) = \frac{N}{4\pi \sin\theta} \cdot \frac{\alpha}{\alpha^2+1} \cdot \frac{\gamma'_p}{\cos^2\theta} \frac{\left[m + \sqrt{1-(m^2-1)\alpha^2}\right]^2}{\sqrt{1-(m^2-1)\alpha^2}}, \qquad \text{(A III.14)}$$

$$\gamma_\pi = \frac{(\gamma'_\pi/\gamma'_p)(\gamma'^2_p + \alpha^2) + \sqrt{\gamma'^2_\pi - 1}\,\sqrt{\gamma'^2_p - 1}\,\sqrt{1-(m^2-1)\alpha^2}}{\alpha^2+1}. \qquad \text{(A III.15)}$$

$\theta > \frac{1}{2}\pi$

$$I(\theta, W_p) = \frac{N}{4\pi \sin\theta} \cdot \frac{\alpha}{\alpha^2+1} \cdot \frac{\gamma'_p}{\cos^2\theta} \frac{\left[m - \sqrt{1-(m^2-1)\alpha^2}\right]^2}{-\sqrt{1-(m^2-1)\alpha^2}}, \qquad \text{(A III.16)}$$

$$\gamma_\pi = \frac{(\gamma'_\pi/\gamma'_p)(\gamma'^2_p + \alpha^2) - \sqrt{\gamma'^2_\pi - 1}\,\sqrt{\gamma'^2_p - 1}\,\sqrt{1-(m^2-1)\alpha^2}}{\alpha^2+1}. \qquad \text{(A III.17)}$$

From eq. A III.3, if $m = 1$, the relation between θ and θ' is:

$$\operatorname{tg}\theta = \frac{1}{\gamma'_p} \operatorname{tg}\frac{\theta'}{2} = \operatorname{tg}\frac{\theta'}{2} \sqrt{\frac{2m_pc^2}{W_{\text{tot}}}},$$

where W_{tot} is given by eq. A III.7.

Half the number of particles in the L-system are within a cone defined by the apex angle $2\theta_{\frac{1}{2}}$. The value of $\theta_{\frac{1}{2}}$ is found from eq. AIII.18 by putting $\theta' = \frac{1}{2}\pi$:

$$\operatorname{tg}\theta_{\frac{1}{2}} = \sqrt{2m_pc^2/W_{\text{tot}}}. \qquad \text{(A III.19)}$$

A IV. The counting rate of cylindrical telescopes assuming a $\cos^2\beta$ distribution of the intensity

We consider fig AI.1 and find the expression for the counting rate of a surface element da within the shaded surface. The beam of particles subtends the solid angle $d\omega$ and its direction of incidence makes the angle u to the vertical. As the telescope points in the zenith direction $u = \beta$. The beam intensity is given by:

$$I = I_0 \cos^2\beta \quad \text{particles/cm}^2\cdot\text{sec}\cdot\text{sterad.} \qquad \text{AIV.1}$$

Thus the contribution to the counting rate from the element da due to particles coming within the solid angle $d\omega$ from the zenith direction β is:

$$d^3\nu = I_0 \cos^2\beta \, da \cos\beta \, d\omega \quad \text{particles/sec.} \qquad \text{AIV.2}$$

This applies to any surface element of the shaded surface. The counting rate of the telescope is consequently:

$$d^2\nu = I_0 \cos^3\beta \, S \, d\omega \quad \text{particles/sec,} \qquad \text{AIV.3}$$

where S is given by eq. AI.1 in appendix I.

Integration over the total solid angle yields:

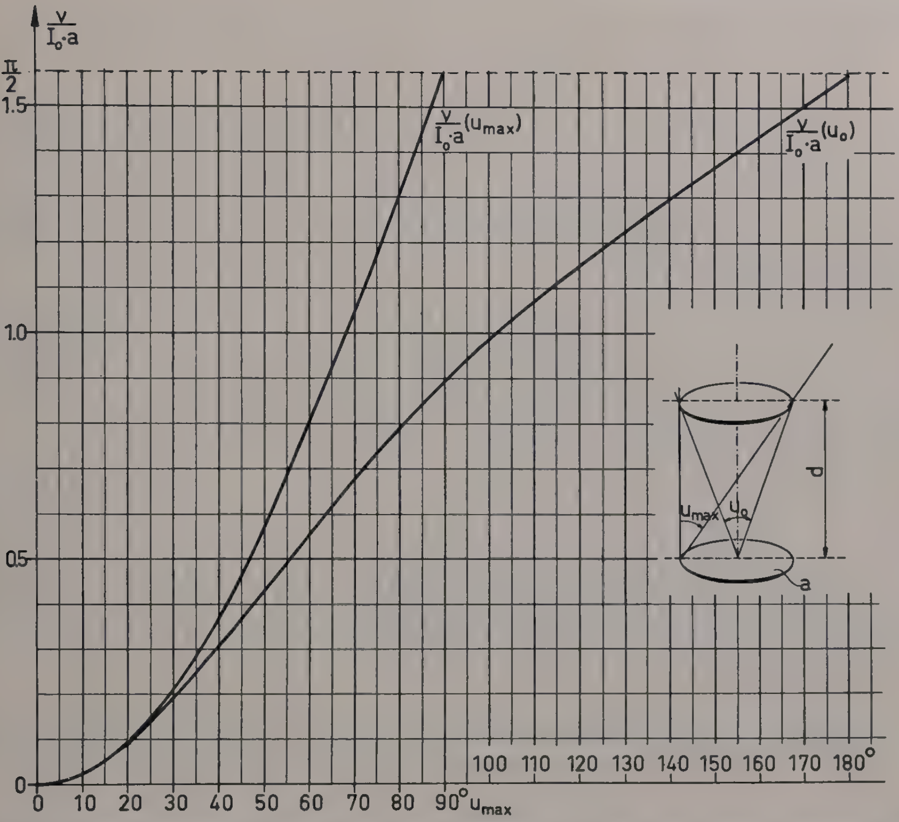

Fig. A IV.1. The variation of counting rate with aperture of a cylindrical telescope assuming the intensity to vary as $\cos^2\beta$ where β is the zenith angle. I_0 is the intensity in the zenith direction.

$$\nu = I_0 \frac{2a}{\pi} \int_{\alpha=0}^{2\pi} \int_{\beta=0}^{\beta_{\max}} \cos^3\beta \left(\varphi_{\max} - \frac{\sin 2\varphi_{\max}}{2}\right) \sin\beta \, d\alpha \, d\beta, \qquad \text{(A IV.4)}$$

where $\cos\varphi_{\max} = C \operatorname{tg} u$ and $C = d/2r = 1/\mu$.

As α is independent of β we get:

$$\nu = I_0 \, 4a \int_0^{\beta_{\max}} \cos^3\beta \left(\varphi_{\max} - \frac{\sin 2\varphi_{\max}}{2}\right) \sin\beta \, d\beta. \qquad \text{(A IV.5)}$$

After change of variable ($\operatorname{tg}\beta = \mu \cdot \cos\varphi$) and dropping the subscript we have:

$$\nu = I_0 \, 4a \int_0^{\pi/2} \frac{\mu^2 \cos\varphi}{(1+\mu^2\cos^2\varphi)^3} \sin\varphi \left(\varphi - \frac{\sin 2\varphi}{2}\right) d\varphi. \qquad \text{(A IV.6)}$$

Integration by parts gives:

$$\nu = I_0\, 4a \Big/_{0}^{\pi/2} \mu^2 f(\varphi)\left(\varphi - \frac{\sin 2\varphi}{2}\right) - I_0\, 4a \int_0^{\pi/2} \mu^2 f(\varphi)\, 2\sin^2\varphi\, d\varphi, \qquad \text{(A IV.7)}$$

where

$$f(\varphi) = \int \frac{\cos\varphi \sin\varphi}{(1+\mu^2\cos^2\varphi)^3}\, d\varphi = \frac{1}{4\mu^2}\, \frac{1}{(1+\mu^2\cos^2\varphi)^2}\,. \qquad \text{(A IV.8)}$$

Eq. AIV.7 is now written:

$$\nu = a\, I_0 \left[\frac{\pi}{2} - \int_0^{\pi/2} \frac{2\sin^2\varphi}{1+\mu^2\cos^2\varphi}\, d\varphi\right]. \qquad \text{(A IV.9)}$$

The solution is (cf. Meyer zur Capellen, *Integraltafeln*, p. 156):

$$\nu = a\, I_0\, \tfrac{1}{2}\pi (1 - \cos u_{\max}). \qquad \text{AIV.10}$$

Eq. AIV.10 has been plotted in fig. AIV.1.

Another telescope configuration has been treated by Newell *et al.* [44]. They have calculated the counting rate of a telescope consisting of two parallel Geiger–Müller tubes. Witmer and Pomerantz [45] have discussed the counting rate of a telescope with rectangular surface.

ARKIV FÖR FYSIK. Bd 14 nr 16

Magnetic deflection of secondary cosmic ray particles in the atmosphere

By Björn Bonnevier

A secondary cosmic ray particle which is formed in the atmosphere moves towards the earth and suffers energy loss during its motion. If it is charged, its motion also depends on the earth's magnetic field. The aim of this paper is to calculate the length and the angular deflection of a particle orbit. Instead of calculating the orbit of a particle moving towards the earth one can obtain the same result by calculating the orbit of a particle with opposite charge moving in the opposite direction.

The problem is as follows: We assume a point at sea level where there is a magnetic field B directed at an angle $(90° - \delta)$ to the zenith direction. δ is the dip angle. A particle starts in the direction T at an angle β to the zenith direction and at an angle γ to the magnetic field as shown in figure 1. As we treat the case of a particle moving upwards, it gains energy during its motion. We want a relation between the length of the particle orbit and the height above sea level. The magnetic field is assumed to be constant throughout the length of the orbit. Scattering in the atmosphere is neglected.

A particle orbit in three dimensional space can be described by the vector $|\xi(s), \eta(s), \zeta(s)|$. The the radius of curvature r is given by

$$\frac{1}{r} = \sqrt{\left(\frac{d^2\xi}{ds^2}\right)^2 + \left(\frac{d^2\eta}{ds^2}\right)^2 + \left(\frac{d^2\zeta}{ds^2}\right)^2}, \tag{1}$$

where s = the length of the arc.

If the particle moves in a homogeneous magnetic field and there is also a force directed tangentially to the particle orbit we have:

$$v_{\|}/v_{\perp} = k = \operatorname{ctg}\delta;$$

$v_{\|}$ = the particle velocity parallel to the magnetic field

$v_{\perp}$ = the particle velocity perpendicular to the magnetic field and positive in anticlockwise direction

k = constant

If the magnetic field is along the ζ-axis we have:

$$\frac{d\zeta^2}{d\xi^2 + d\eta^2} = k^2$$

and

$$ds^2 = (1+k^2)\,[d\xi^2 + d\eta^2].$$

Thus we get:

$$\frac{d\eta}{ds} = \sqrt{\frac{1}{1+k^2} - \left(\frac{d\xi}{ds}\right)^2}; \quad \frac{d\zeta}{ds} = \frac{k}{\sqrt{1+k^2}}, \tag{2}$$

and after derivation and substituting in [1] we arrive at:

$$\frac{1}{r} = \pm\frac{d^2\xi}{ds^2}\sqrt{\frac{1}{1-(1+k^2)\,(d\xi/ds)^2}}. \tag{3}$$

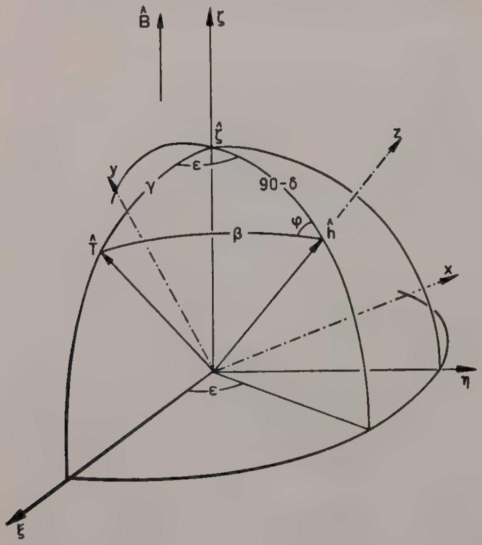

Fig. 1. Coordinates used in this deduction.

In order to get $r_\perp$ the radius of curvature of the projection of the orbit in the $\xi\eta$-plane we put:

$$\left.\begin{aligned} 1/r_\perp &= \sqrt{d^2\xi/d\sigma^2 + d^2\eta/d\sigma^2},\\ d\sigma^2 &= d\xi^2 + d\eta^2 = ds^2/(1+k^2).\end{aligned}\right\}$$

The derivatives $d^2\xi/d\sigma^2$ and $d^2\eta/d\sigma^2$ can be expressed in terms of $d^2\xi/ds^2$ and $d\xi/ds$. We then get:

$$1/r_\perp = (1+k^2)/r.\text{(1)} \tag{4}$$

In order to find another expression for $r_\perp$ we make the following approach. Let $W(s)$ denote the kinetic energy of a particle and W_0 its rest energy. Then the particle momentum is: $p = [W(W+2W_0)]^{\frac{1}{2}}/c$.

As $p_{\parallel}/p_\perp = k$ we get $p_\perp = p/\sqrt{1+k^2}$ and

$$r_\perp = \frac{p_\perp}{|Ze|B} = \frac{[W(W+2W_0)]^{\frac{1}{2}}}{c|Ze|B} \cdot \frac{1}{\sqrt{1+k^2}}\,. \tag{5}$$

We have now obtained two expressions for $r_\perp$, (4) and (5). Putting these equal we get:

$$\frac{1}{r_\perp} = \frac{c|Ze|B}{[W(W+2W_0)]^{\frac{1}{2}}}\sqrt{1+k^2} = \pm\frac{d^2\xi}{ds^2}\,\frac{1+k^2}{\sqrt{1-(1+k^2)(d\xi/ds)^2}}\,. \tag{6}$$

---

(1) This result could also have been obtained with the relation between the radius of curvature for a surface in a certain direction and the main radii of curvature.

The ζ-axis has already been chosen so that it has the same direction as the magnetic field. Now we choose the ξ-axis in such a way that the $\xi\zeta$-plane is a tangential plane to the particle orbit at sea level. The origin in our coordinate system is this point of contact. For a particle starting from the origin we take $ds > 0$. At the origin $d\xi/ds > 0$ gives the direction of the ξ-axis and the choice of a righthanded system gives the η-axis. The special case $d\xi/ds = 0$ at the origin is trivial as the motion is then parallel to the magnetic field. We thus choose the minus sign in eq. (6). In (6) we make the substitution:

$$t = (d\xi/ds)\sqrt{1 + k^2}$$

and get the integrals

$$\int_1^t \frac{-dt}{\sqrt{1-t^2}} = \arccos t = c|Ze|B \int_0^s \frac{ds}{\sqrt{W(W+2W_0)}}, \tag{7}$$

where the energy W is a function of the path length s.

In order to find a relation between W and s, when we treat the case of a secondary cosmic ray particle moving through the atmosphere, we consider the motion along the short path length ds. The energy gain is $dW/ds = \varrho(dW/\varrho ds) = \varrho q$, where ϱ = the density of the penetrated matter. The atmosphere is assumed to be in static and thermal equilibrium thus $\varrho = \varrho_0 e^{-h/l}$, where h = height above sea level, l = scale height and ϱ_0 = air density at sea level. $dW/\varrho ds = q$ is given for different energies and particles for example in W. Heisenberg, *Kosmische Strahlung*, Berlin 1953. To simplify the calculation, q is taken as a constant which is a good approximation in the relevant energy range. Thus we have

$$\left.\begin{aligned} dW &= q\varrho_0 e^{-h/l}\,ds \\ \text{or}\qquad W &= W_1 + q\varrho_0 \int_0^s e^{-h/l}\,ds \end{aligned}\right\} \tag{8}$$

which enters into the integral (7).

To solve this integral we have to make a zero order approximation for the desired function $h(s)$. We put $h = s\cos\beta$. It is then possible to integrate and obtain $d\xi/ds$ as a function of s. Using $d\xi/ds$ we get dh/ds and one more integration gives a first order approximation to $h(s)$. In principle we could go further to higher order approximations, but the first order approximation is good enough. Now we have

$$\arccos t = c/Ze/B \int_0^s \frac{ds}{\sqrt{W(W+2W_0)}} = \frac{cl/Ze/B}{\cos\beta} \int_{W_1}^{W_2} \frac{dW}{\sqrt{W(W+2W_0)(W_3-W)}}$$

with the substitution:

$$W = W_1 + (W_3 - W_1)\left[1 - \exp\left(-\frac{s\cos\beta}{l}\right)\right],$$

where W_1 = particle energy at sea level
W_2 = particle energy at path length s
$W_3 = W_1 + q\varrho_0 l/(\cos\beta)$
$W_3 - W_1$ = the energy loss of a particle moving from the top of the atmosphere to sea level.

Integration gives:

$$\frac{d\xi}{ds} = \frac{1}{\sqrt{1+k^2}} \cos\left\{\frac{cl/Ze/B}{\cos\beta\sqrt{W_3(W_3+2W_0)}}\left[\operatorname{ar\,cosh}\left(-\frac{W_3+W_0}{W_0} + \right.\right.\right.$$

$$\left.\left.\left. + \frac{W_3(W_3+2W_0)}{W_0(W_3-W_1)\,e^{-(s\cos\beta)/l}}\right) - \operatorname{ar\,cosh}\left(-\frac{W_3+W_0}{W_0} + \frac{W_3(W_3+2W_0)}{W_0(W_3-W_1)}\right)\right]\right\}$$

$$= \frac{1}{\sqrt{1+k^2}}\cos\theta = \sin\gamma\cos\theta, \tag{9}$$

where θ is the expression within the brackets.

Now we want to express dh/ds in terms of $d\xi/ds$. In addition to the angles $\beta\gamma\delta$ earlier introduced we need the angles:

ε = the angle between the $\zeta - h$ and $\zeta - \xi$ planes;
φ = the angle between the $\zeta - h$ and $h - T$ planes.

From equations (2) and (9)

$$\left.\begin{aligned} d\xi/ds &= \sin\gamma\cos\theta, \\ d\eta/ds &= \pm\sin\gamma\sin\theta, \\ d\zeta/ds &= \cos\gamma. \end{aligned}\right\}$$

The plus sign applies for a positive particle moving towards the earth. Since

$$\hat{h} = [\cos\delta\cos\varepsilon;\ \cos\delta\sin\varepsilon;\ \sin\delta]$$

we get

$$dh/ds = (d\xi/ds)\cos\delta\cos\varepsilon + (d\eta/ds)\cos\delta\sin\varepsilon + (d\zeta/ds)\sin\delta.$$

Using the spherical sine and cosine theorems:

$$\cos\beta = \cos\delta\sin\gamma\cos\varepsilon + \sin\delta\cos\gamma,$$

$$\cos\gamma = \sin\beta\cos\delta\cos\varphi + \cos\beta\sin\delta,$$

$$\sin\gamma\sin\varepsilon = \sin\beta\sin\varphi;$$

to eliminate ε and γ we get:

$$dh/ds = (\cos\beta\cos^2\delta - \sin\beta\sin\delta\cos\delta\sin\alpha)\cos\theta \pm$$

$$\pm\sin\beta\cos\delta\sin\varphi\sin\theta + \cos\beta\sin^2\delta + \sin\beta\sin\delta\cos\delta\cos\varphi. \tag{10}$$

In the same way we can find derivatives with respect to s in other directions, which are of interest in the deflection problem.

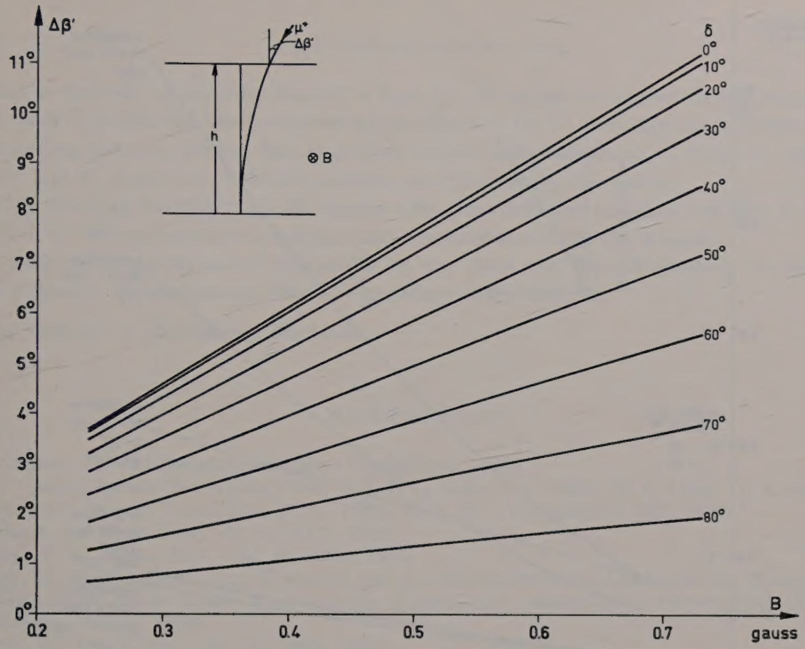

Fig. 2. Deflection of μ-mesons arriving at sea level from the zenith direction.

$$dx/ds = -\sin\beta\sin\varphi\cos\theta \pm (\cos\beta\cos\delta - \sin\beta\sin\delta\cos\varphi)\sin\theta \tag{11}$$

Knowing dx/ds and dh/ds, dy/ds is given by the relation

$$(dx/ds)^2 + (dy/ds)^2 + (dh/ds)^2 = 1.$$

Explicitly

$$\begin{aligned} dy/ds = {} & (\sin\beta\sin^2\delta\cos\varphi - \cos\beta\sin\delta\cos\delta)\cos\theta \mp \\ & \mp \sin\beta\sin\delta\sin\varphi\sin\theta + \sin\beta\cos^2\delta\cos\varphi + \cos\beta\sin\delta\cos\delta. \end{aligned} \tag{12}$$

We are also interested in the relative difference between the path length in the magnetic field and the path length without magnetic field.

This is:

$$\begin{aligned} \frac{s\cos\beta - h}{s\cos\beta} = {} & 1 - \sin^2\delta - \operatorname{tg}\beta\sin\delta\cos\delta\cos\varphi - \\ & - \frac{1}{s}\left[(\cos^2\delta - \operatorname{tg}\beta\sin\delta\cos\delta\cos\varphi)\int_0^s \cos\theta\, ds \mp \operatorname{tg}\beta\cos\delta\sin\varphi\int_0^s \sin\theta\, ds\right]\cdot \end{aligned} \tag{13}$$

We may be interested in performing the integration:

$$\frac{1}{2\pi}\int_0^{2\pi} \frac{s\cos\beta - h}{s\cos\beta}\, d\varphi = 1 - \sin^2\delta - \frac{\cos^2\delta}{s}\int_0^s \cos\theta\, ds, \tag{14}$$

where the dependence of β is included in $\cos\theta$.

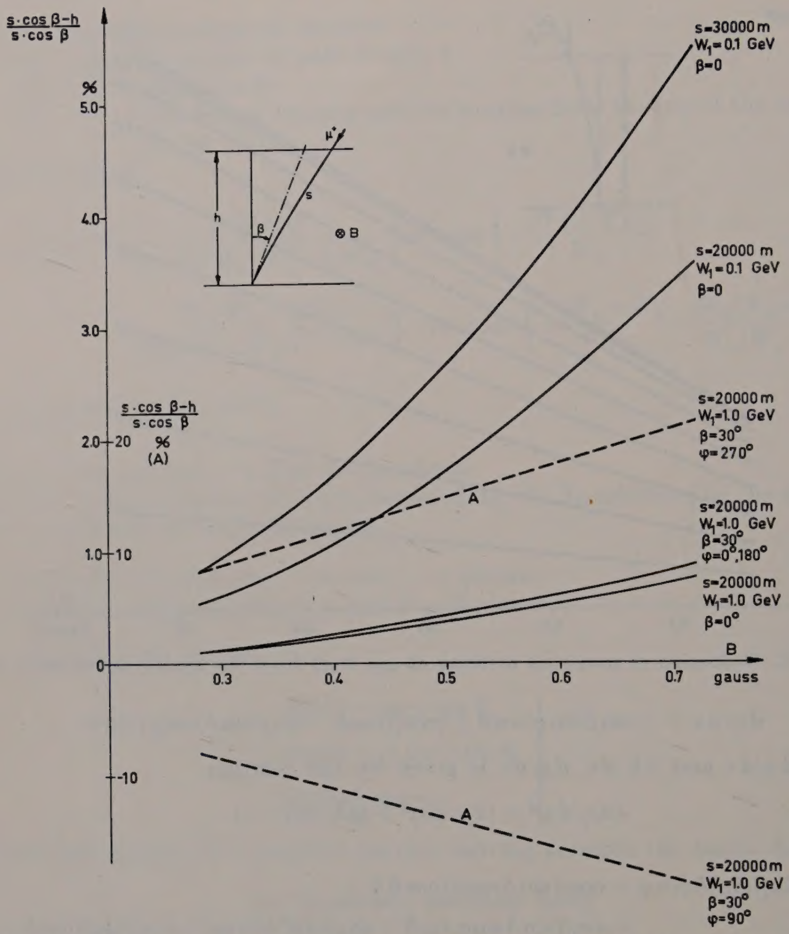

Fig. 3. Relative change of path length for a μ-meson caused by deflection in a magnetic field.

In fig. 2 the deflection of μ-mesons which arrive at sea level from the zenith direction and have started from a height of 20 km have been plotted as a function of δ and B. The particle energy W_1 is 1 GeV at sea level. The values have been obtained by taking $\Delta\beta' = \arccos(dh/ds)$ from eq. (10), with

$$\begin{aligned} \beta &= 0, \\ l &= 7970 \text{ m}, \\ \varrho_0 &= 0.001293 \text{ g/cm}^3, \\ q &= 2 (\text{MeV cm}^2/\text{g}), \\ W_0 &= 0.107 \text{ GeV} \quad \text{in formula (9) for } \theta. \end{aligned}$$

The curves approximate very closely to straight lines.

$(s\cos\beta - h)/(s\cos\beta)$ have been plotted from eq. (13) as a function of B in fig. 3. The parameters are s, W_1, β and φ. The dip angle $\delta = 0$. The values given in fig. 3 justify the approximations made earlier by putting $s = h\cos\beta$.

ACKNOWLEDGEMENTS

I want to express my warmest thanks to Prof. H. Alfvén for his interest in and support of the present work. I should also like to express my gratitude to Dr. N. Herlofson for countless stimulating discussions and good advice. Thanks are due to Drs. A. E. Sandström, L. Block, A. Dattner, D. Eckhartt and E. Åström for valuable criticism and interesting discussions.

Mrs. K. Forsberg has drawn all the figures with great skill and patience and Mrs. J. Dahlberg and Mr. J. C. Wilson have given valuable assistance in correcting the English.

The work has been supported financially by the *Knut and Alice Wallenberg Foundation* and *Statens Tekniska Forskningsråd*, which is gratefully acknowledged.

Royal Institute of Technology, Stockholm.

REFERENCES

1. Störmer, C., Videnskabs-selskabet i Christiania, 1904.
—— Astrophysica Norvegica, Oslo. Vol. I, 1, 1934; I, 4, 1935; II, 1, 1936; II, 4, 1937.
2. Lemaître, G. and Vallarta, M. S., Phys. Rev. *49*, 719, 1936; *50*, 493, 1936.
3. Firror, J., Phys. Rev. *94*, 4, 1017, 1954.
4. Jory, F. S., Phys. Rev. *103*, 4, 1068, 1955.
5. Lüst, R., Schlüter, A., and Katterbach, K., Nachrichten der Akademie der Wissenschaften in Göttingen, Matemaitsch-Physikalische Klasse. 11a. Matematisch-Physikalisch-Chemische Abteilung. Nr. 8, 1956.
6. Lüst, R., Phys. Rev. *105*, 6, 1827, 1957.
7. Heisenberg, W., Kosmische Strahlung. Springer Verlag, Berlin, 1953.
8. Wilson, J. G., Progress in Cosmic Ray Physics, I. North-Holland Publishing Company, Amsterdam, 1952.
9. Malmfors, K. G., Arkiv för Matematik, Astronomi och Fysik *32A*, No. 8, 1945.
10. Brunberg, E. Å. and Dattner, A., Tellus *5*, 2 and 3, 1953.
11. Lemaître, G. and Vallarta, M. S., Phys. Rev. *43*, 2, 87, 1933.
12. Swann, W. F. G., Phys. Rev. *44*, 224, 1933.
13. Jánnossy, L., Cosmic Rays. Clarendon Press, Oxford, 1948.
14. Åström, E., Tellus *8*, 2, 1956.
15. Brunberg, E. Å., Tellus *8*, 2, 1956.
16. Vernov, S. N., Kulikov, A. M., and Feinberg, Y. L., Dok. Akad. Nauk. *80*, 6, 1951.
17. Sandström, A. E., Awaiting publication in Proceedings of the Guanajuato Conference 1955.
18. Rossi, B., High-Energy Particles. Prentice-Hall Physics Series, New York, 1952.
19. Sands, M., Phys. Rev. *77*, 2, 1949.
20. Bowen, I. S., Millikan, R. A., and Neher, H. V., Phys. Rev. *53*, 855, 1938.
21. Gangnes, A. V., Jenkins, J. F., and van Allen, Phys. Rev. *75*, 57, 1949.
22. Vidale, M. L. and Schein, M., Nuovo Cimento *VIII*, 10, 1951.
23. Winckler, J. R., and Stroud, W. G., Phys. Rev. *76*, 8, 1012, 1949.
24. Vernov, S. N., Kulikov, A. M., and Charakch'yan, A. N., Dok. Akad. Nauk. *85*, 3, 525, 1952.
25. Singer, S. F., Phys. Rev. *77*, 5, 1950.
26. Glaser, R. G., Haskin, D. M., Schein, M., and Lord, J. J., Phys. Rev. *99*, 5, 1555, 1955.
27. Cocconi, G., Private communication.
28. Greisen, K., Private communication.
29. Camerini, U., Lock, W. O., and Perkins, D. H., Publication in ref. 8.
30. Bradt, H. L., Kaplan, M. F., and Peters, B., Helv. Phys. Acta *23*, p. 24, 1950.
31. Brunberg, E. Å. and Dattner, A., Tellus *6*, 1, 1954.
32. Ascoli, G., Phys. Rev. *79*, p. 812, 1950.
33. Johnson, T. H., Phys. Rev. *56*, 226, 1939.
34. Bowen, I. S., Phys. Rev. *45*, 349, 1934.
35. Owen, B. G. and Wilson, J. G., Proc. Phys. Soc. *A 64*, 417, 1951.
36. Eckhartt, D., Private communication.
37. Sarabhai, W., Desai, V. D., and Venkatesan, D., Nature *171*, 122, 1953.

38. Greisen, K., Phys. Rev. *61*, 212, 1942.
39. Montgomery, D. J. X., Cosmic Rays. Princeton University Press, Princeton, New Jersey, p. 169, 1949.
40. Neher, H. V., Phys. Rev. *78*, 6, 674, 1950.
41. Simpson, J. A., Fonger, W., and Treiman, S. B., Phys. Rev. *90*, 5, 934, 1953.
42. Fonger, W. H., Phys. Rev. *91*, 2, 351, 1953.
43. Jahnke, E. and Emde, F., Tables of Functions. Dover Publications, New York, 1945.
44. Newell, H. E. and Pressly, E. C., Rev. Sc. Instr. *21*, 11, 918, 1950.
45. Witmer, E. E. and Pomerantz, M. A., J. Franklin Inst. *246*, 293, 1948.
46. Kaplon, M. F., Peters, B., Reynolds, H. L., and Ritson, D. M., Phys. Rev. *85*, 295, 1952.

Tryckt den 24 september 1958.

Uppsala 1958. Almqvist & Wiksells Boktryckeri AB